GLASS WELDING USING CUSTOM DEVELOPED FEMTOSECOND FIBER LASER FOR MICROFLUIDIC DEVICE DEVELOPMENT

by

Gizem Alpakut

B.S., Physics, Boğaziçi University, 2016

Submitted to the Institute for Graduate Studies in
Science and Engineering in partial fulfillment of
the requirements for the degree of
Master of Science

Graduate Program in Physics

Boğaziçi University

2020

ACKNOWLEDGEMENTS

I would like to thank to my thesis advisor Prof. Mehmet Burçin Ünlü for his support, encouragement, and guidance, throughout my M.S thesis study. Without his motivations and enthusiasm, it would not have been possible to write the thesis.

I would like to thank Dr. Uğur Parlatan for valuable his guidance and constructive feedbacks. I have learned a lot from him.

I would like to thank to my friend Dr. Nasire Uluç for her helpful discussions and sharing her abundance of knowledge.

I especially would like to thank Dr. Seydi Yavaş for his guidance and support during my studies.

I would like to thank my family for their endless support during my studies.

I would also like to thank my thesis committee members for sparing their valuable time and for their reviews and corrections on my thesis.

The financial support during my studies from TUBITAK (Project number 118S113 and 116F142), Turkish Ministry of Development are also gratefully acknowledged.

ABSTRACT

GLASS WELDING USING CUSTOM DEVELOPED FEMTOSECOND FIBER LASER FOR MICROFLUIDIC DEVICE DEVELOPMENT

Microfluidic chips made of different materials are utilized in numerous examination fields, as they make it possible to screen and study distinctive processes that happen in minuscule sizes. A typical microfluidic device consists of two plates, one with a surface with microstructures, the other covers the top of the channel structures to isolate the assembly from the environment. Many of the traditional methods used to combine these two plates require preliminary preparation, which adds time, cost and energy to production, but the result can still be problematic in terms of repeatability and longevity. In this thesis, it is aimed to produce microchannels on glass samples and to join them together using a femtosecond laser. In this way, application-specific modifications, repeatable and faster chip production may be possible. We have built a femtosecond fiber laser system with adjustable output parameters for the production of microchannels and welding of glasses. The central wavelength of the developed laser is 1030 nm and the pulse duration can be adjusted between 250 fs -10 ps, pulse energy up to 5 μJ and repetition frequency between 150 - 400 kHz independently from each other. Using this fiber laser system, we investigated the most suitable parameters for glass welding. For this, we have built up two experimental setups with scanning systems that can operate at m/s and mm/s speeds. We examined the effects of laser pulse energy, repetition rate and scanning speed for welding of glasses with different thicknesses and types. We have achieved successful results in welding experiments with spiral and raster scanning on borosilicate and aluminosilicate glasses with different thicknesses. Durability tests of the welded glasses were carried out with a press test machine and preliminary results for microfluidic device development were presented.

ÖZET

MİKROAKIŞKAN ÇİP GELİŞTİRİLMESİNE YÖNELİK AMACA ÖZEL FEMTOSANİYE FİBER LAZERLE CAM BİRLEŞTİRME

Farklı malzemelerden yapılan mikroakışkan çipler, çok küçük boyutlarda meydana gelen ayırt edici süreçleri taramayı ve incelemeyi mümkün kıldığından çok sayıda inceleme alanında kullanılırlar. Tipik bir mikroakışkan cihaz, biri mikro yapılara sahip bir yüzeye sahip, diğeri ise düzeneği çevreden izole etmek için kanal yapılarının üstünü kaplayan iki plakadan oluşur. Bu iki plakayı birleştirmek için kullanılan geleneksel yöntemlerin çoğu, üretime zaman, maliyet ve enerji ekleyen ön hazırlık gerektirir, ancak sonuç, tekrarlanabilirlik ve uzun ömür açısından yine de sorunlu olabilir. Bu tezde cam numuneler üzerinde mikrokanalların üretilmesi ve femtosaniye lazer kullanılarak birleştirilmesi amaçlanmıştır. Bu şekilde uygulamaya özel modifikasyonlar, tekrarlanabilir ve daha hızlı çip üretimi mümkün olabilir. Mikro kanalların üretimi ve camların kaynağı için ayarlanabilir çıktı parametrelerine sahip bir femtosaniye fiber lazer sistemi kurduk. Geliştirilen lazerin merkezi dalga boyu 1030 nm olup, atım süresi 250 fs -10 ps aralığında, atım enerjisi 5 μJ'e kadar ve tekrar frekansı 150 - 400 kHz arasında ayarlanabilmektedir. Bu fiber lazer sistemini kullanarak camların birleştirilmesi için en uygun parametreleri araştırdık. Bunun için, m/s ve mm/s hızlarında çalışabilen tarama sistemleri ile iki deneysel düzenek oluşturduk. Farklı kalınlık ve tipteki camların kaynağı için lazer atım enerjisi, tekrar sıklığı ve tarama hızının etkilerini inceledik. Farklı kalınlıktaki borosilikat ve alüminosilikat camlarda spiral ve ızgara tarama şekli ile camı birleştirdiğimiz deneylerde başarılı sonuçlar elde ettik. Birleşmiş camların dayanıklılıklarını basma testi ile test ettik ve mikroakışkan çip yapımı için ön sonuçlarımızı sunduk.

TABLE OF CONTENTS

LIST OF FIGURES

LIST OF TABLES

LIST OF SYMBOLS

B	B-integral of the pulse
G	Total gain
D_2	Intracavity dispersion
L_2	Intracavity fiber length
n_2	Nonlinear refractive index
β_2	Group velocity dispersion
γ	Nonlinearity parameter
λ	Wavelength
ω_p	Plasma frequency
ϕ_s	Soliton phase
τ	Pulse width

LIST OF ACRONYMS/ABBREVIATIONS

2D	2 Dimensional
3D	3 Dimensional
AOM	Acousto Optic Modulator
COC	Cyclic-olefin-copolymer
CCD	Charge Coupled Device
CMOS	Complementary Metal Oxide Semiconductor
CPA	Chirped Pulse Amplification
DAC	Digital to Analog Converter
dB	Decibel
DC	Double Clad
FPGA	Field Programmable Gate Array
FWHM	Full Width at Half Maximum
GVD	Group Velocity Dispersion
HAZ	Heat-Affected Zone
HWP	Half Wave Plate
kW	Kilo Watt
LD	Laser Diode
LoC	Lab-on-a-Chip
MEMS	Microelectromechanical Systems
MPC	Multi-mode Pump Combiner
N.A.	Numerical Aperture
NPE	Nonlinear Polarization Evolution
NPR	Nonlinear Polarization Rotation
OoC	Organ-on-a-Chip
PC	Polycarbonate
PDMS	Poly-di-methyl-siloxane
PLA	Polylactic acid
PMMA	Poly- methyl-methacrylate

PBS	Polarizing Beam Splitter
PoC	Point-of-Care
QWP	Quarter Wave Plate
RF	Radio Frequency
RIE	Reactive Ion Etching
SLE	Selective Laser Etching
SPM	Self-Phase Modulation
TEC	Thermoelectric Cooler
TW	Tera Watt
WDM	Wavelength Division Multiplexer
YB	Ytterbium

1. INTRODUCTION

1.1. Microfluidic Chips for Diagnosis

Microfluidic chips are used in many industrial and research areas in a broad range of applications, especially in chemistry, biology, medicine and pharmacology [1–5]. They provide many advantages over conventionally designed systems thanks to their compact size. These devices make it possible to specifically track and examine different physical, chemical and biological processes occurring at very small (sub-micron) length scales [1]. Working with these small quantities naturally decreases the amount of samples which are needed for the experiment. Most of the time, less than 10 μl of fluids and test materials with an appropriate concentration of this substance are more than enough. Such small volumes reduces the cost of samples required for testing. Another advantage of working with these devices is that multiple operations can be done simultaneously thanks to the reduced space required for each circuit. The time needed for analysis of each circuit is reduced with the use of small amount of samples, providing high-throughput solution. These devices, for example, allow to detect single cell [6, 7], analyze pathogens [8], develop new antibiotics [9], or even mimic human and animal [10]. As they allow these operations to be carried out on a small set-up, Lab-on-a-chip (LoC) devices, Organ-on-a-Chip (OoC) devices, and Point-of-Care (PoC) medical diagnostic tools are used by biochemists, pharmacologists, clinicians and medical staff. Since they are completely sealed, they reduce sample contamination while providing a boundary between an administrator and an examined material that occasionally can be hazardous.

A typical microfluidic device is made of two plates, one of them has microfluidic channels on its surface, and the other one has inlet ant outlet holes. Plate with the inlet/outlet ports is used as a cover and bonded to the other plate to prevent any leakage during the fluid flows. The operating logic of these systems is very simple. Desired sample is injected into the channel through an inlet. Depending on the analysis, sample interacts with the channels which are modified and leaves the microfluidic

system through the outlet. For example, according to the application, the surface of the channels may be coated with the desired element, the protein may be bound, or made hydrophobic. Typically, the cover plate is transparent and must be appropriately attached to the other plate such that the device is leak-proof and the the infused liquids can stream only within the area of a microfluidic pattern. With the integration of various electronic circuits into the system, they may also have various features such as controlled automatic flow and controlled temperature.

Microfluidic devices can be made from a wide scope of materials, such as transparent silicone elastomer (poly-di-methyl-siloxane (PDMS)), thermoplastics (e.g. polymethyl-methacrylate (PMMA), polycarbonate (PC), cyclic-olefin-copolymer (COC)), renewable polymers (e.g. polylactic acid (PLA)), chromatography paper, photoresist, hydrogels, glass and silicon [11–14]. Depending on the material, patterns of a microfluidic device can be generated by using soft lithography, casting, injection moulding, hot embossing, wax printing, inkjet printing, mechanical milling, 3D printing, two-photon polymerisation, laser micro-machining, or etching [15–19]. Regardless of the material used, covering the top of the channel structures is a necessary condition to isolate the assembly from the environment. The two plates may be permanently glued to each other using adhesives, although this technique has a strong disadvantage that during the bonding, glue may infiltrate microchannels and obstruct the flow pattern. More traditional approaches require the use of intermediate layers (SU-8 photoresist, parylene, polyimide), heat (so-called thermal bonding) or electric field (so-called anodic bonding) [15, 16, 20]. However, both of these techniques need specialized machinery and space, such as clean room, wafer bonding machine, furnace, etc, which significantly raises the expense of making microfluidic devices.

1.2. Glass Microfluidic Chips

Compared to other materials used for microfluidic device fabrication, glass offer a unique combination of optical, mechanical, thermal, chemical and electrical properties. It has high optical transparency, strong strength, thermal resilience, high tolerance to humidity, electrical insulation, chemical inertness to other fluids, biocompatibility

and well-defined surface chemistry. These desirable characteristics of glass make it practically perfect material for microfluidic devices, but unfortunately increase the complexity of joining. Although there are proven technologies for glass joining, these technologies have certain limitations so that the specific use case of the final component needs to be considered. Unfortunately, the traditional manufacturing of microfluidic devices using glass substrates is a complicated, requiring multi-step procedures that include specific manufacturing techniques and tools [15–17]. Each operation introduced to the manufacturing technique thus influences the time and money spent. The two popular methods used to produce microfluidic patterns on glass substrates are reactive ion etching (RIE) and wet (chemical) etching, which respectively strip the substance using chemically reactive plasma and liquid chemicals called etchants. All of these approaches involve the use of custom-designed masks, which would undoubtedly add time, costs and energy to produce a microfluidic patterns on a plate. A mixture of spin coating and direct laser writing, physical vapor deposition and direct laser writing, photolithography and etching, or photolithography and electroplating may be used to create such masks. Beside these, one of the relatively fast methods among current techniques rely on adhesives or interlayers that can suffer from problems like outgassing and ageing [21].

Microfluidic patterns may also be produced directly on a glass surface using a CO_2 or ultrashort pulsed lasers [22, 23]. Combined with a galvo-scanning device and a computer-aided software, generation of complex patterns with different depths and widths is possible. This is done by changing the laser parameters and the distance of the material from the focusing optics. After the structures are created on the surface, a second glass is closed to the first one by laser welding. Ultrafast lasers can also be used for the generation of three-dimensional (3D) microfluidic patterns inside glass materials using selective laser etching (SLE) method [24]. Selective laser etching is especially desirable as it avoids the use of a physical mask and additional fabrication steps such as bonding the glass plates together. But it is still time consuming considering the etching process and it requires the use of hazardous etchants, tools to heat these etchants and keep them at a constant temperatures.

1.3. Femtosecond Laser as a Tool for Glass Microfluidic Chip Manufacturing

In recent years, femtosecond laser glass processing has received considerable interest for the applications that use glass such as photonics, displays, and optoelectronics [25, 26]. It enabled glass micromachining and glass-to-glass bonding become a simple, fast and repeatable process [27,28]. By this means, in microfluidic chip production, femtosecond laser processing has also decreased the challenges in manufacturing, as it can be used both for the creation of micro patterns and for the packaging of a glass chip via welding process. Due to the shortness of the pulse duration, the mechanism of interaction with the material allows it to work more precisely compared to other long pulse lasers. Table 1.1 shows the laser-material interaction mechanisms for different pulse durations and corresponding precision qualities.

The basic principle of femtosecond-pulsed glass laser processing is to cause nonlinear absorption which enables direct photo-ionization in the material only at very high laser intensity at a range of TW/cm^2. Under this conditions, glass absorbs photons directly, resulting a local melting and structural changes at the focus point. Importantly, as there is no need to use an intermediate layer for the heat transfer, femtosecond laser direct writing is one of the most revolutionary applications for the femtosecond laser manufacturing.

Considering the microfluidic chip technology, although it is not new, the use of these devices is quite few for having some optimization problems. The fact that a new optimization process is required for each study can be seen as a complicating effect on the studies. But its advantages are significant enough that such a disadvantage can be easily overlooked. Comparing all methods of the microfluidic device fabrication, femtosecond pulsed lasers appear as a tool that offers the fast and repeatable solution for optimization processes which may be required over and over.

Femtosecond laser direct writing and glass welding brings several other advantages for microfluidic device manufacturing. The creation of channel structures is way faster

Table 1.1. Comparison of precision quality and laser-material interaction mechanisms for lasers with different pulse durations

	Femtosecond Laser	**Picosecond Laser**	**Nanosecond Laser**	**Microsecond Laser**
Duration	10^{-15} s	10^{-12} s	10^{-9} s	10^{-6} s
Interaction mechanism with the material	Photo-ionization and avalance ionization heat up the electrons	Avalance ionization, thermalization of electrons, thermodynamic processes	Thermodynamic and photothermal processes	Thermodynamic and photothermal processes
Precision quality	Highest micromachining precision	High micromachining precision	Low quality micromachining	Low quality micromachining
Precision size	nm	um	larger sizes	larger sizes

and reproducible than all traditional methods. It provides bonding of the base material without any surface treatment which preserves its high chemical resistance. Since the dimensions of the weld lines are directly related to the laser parameters used, they can be adjusted according to the application without damaging the microfluidic channels. Finally, it has a higher bonding strength than other bonding methods [29–31]. This is important when working with microfluidic channel structures because glasses with poor bonding strength can flex and cause leakage due to the pressure created by the injected liquid.

2. FEMTOSECOND FIBER LASER SYSTEM DEVELOPMENT FOR GLASS WELDING

2.1. Introduction

On the technology side, ultrafast optics is the branch of optics dealing with the generation, manipulation, shaping, amplification as well as the applications of the pulses with very high peak powers (>kW) and low pulse durations (<10 ps). The ultrafast definition is evolving in years, beginning from picoseconds to femtoseconds, and in recent years down to attoseconds. In this thesis's context, we imply pulses less than ten picoseconds by ultrafast pulses or ultrashort pulses since this is seen as a threshold for most nonlinear laser-material interaction processes.

Long before the invention of fiber lasers, processes taking place in ultrafast time-scales have been investigated in optical fibers, and prominent phenomena in these time-scales have already been observed [32]. This investigation's primary motivation was to understand the basics behind the low-power thresholds of nonlinear interactions and the long lengths of optical fibers in use, especially in the telecommunication field, and overcome the challenges by designing the fibers and fiber-based systems according to these processes. However, before the arrival of the fiber lasers, bulk, expensive and hard-to-operate ultrafast sources such as dye lasers and solid-state lasers were used to investigate the femtosecond pulse phenomena in optical fibers and the research was limited to a few research laboratories around the world. After more than 25 years of research, ultrafast fiber technology matured enough to be used in generating femtosecond pulses in a more compact, robust, easier-to-operate, and cost-effective manner. Although this time scale looks long, fiber lasers are one of the fastest transitioned laser type from the research laboratory to the industry owing to the implementation of many already-built fiber components and optical fibers mostly for telecommunication applications during the telecom boom in 1990s, which enabled reliable laser designs compared to other laser technologies. Besides, by the advancement of the optical fibers with high

gain (>30 dB) as well as high power laser diodes coupled into fiber (pigtailed) to pump these gain mediums made it possible to build all-fiber amplifier designs, which reduced the complexity of the amplification scheme of the ultrafast pulses that was previously suffering from the optomechanical alignment necessities in addition to the large footprint. Currently, ultrafast fiber lasers began to be utilized in many applications in both scientific and industrial domain such as nonlinear microscopy [33], micromachining [34], ophthalmology [35], optical telecommunications [36] and metrology systems [37].

2.1.1. Fiber Technology

The ultrafast fiber laser technology was not experimentally possible until the invention of rare-earth-doped single-mode fibers [38], single-mode fiber lasers that are pumped via laser diodes [39] and lastly fiber-based amplifiers [40]. These technologies made it possible to build fiber lasers with high bandwidths, high enough power levels, and robust pulsed operation. Silica is a crucial host material for the development progress of fiber lasers owing to its chemical inertness, high optical transparency, and low vulnerability of optical facet damage. The waveguide scheme that the fibers are offering provides the perfect medium to obtain high levels of optical gain. Unlike crystal-based gain mediums in solid-state amplifiers, extended length of fiber amplifiers allows for the efficient cooling of the gain medium easily. Another advantage over solid-state amplifiers is that the distributed heat of the gain medium architecture prevents the thermal lensing which is one of the limiting factors to achieve high gain and hence high average power in conventional ultrafast solid-state laser amplifiers. Thus, the fiber amplifiers do not suffer thermal lensing induced beam distortions up to 100 μm core diameters. These thermal advantages led to advantageous amplifier designs, especially after the development of double-clad fibers. The signal in the core is amplified by the pump light coupled to the cladding [41]. Since the cladding of the fibers is high in numerical aperture, it allows the usage of multimode high-power diode lasers with very high average powers, which paved the way for the high average power fiber laser. After this development, achievable average power limitation from a fiber laser was jumped in orders of magnitude levels, and the kW range amplifiers currently operating [42].

However, the gain mediums that were developed were mostly Nd-doped and Er-doped fibers, which are relatively inefficient for high power amplification due to low doping concentration that is achievable in these fibers. Hence, the introduction of Yb-doped fibers was another vital advent toward the high-power amplification [43]. Yb offers much better solubility in glass host compared to Er and Nd, and can reach much higher doping levels comparing to other doping materials with minimum side-effects [44]. Yb-doping was so successful that the absorption levels of 90 dB/cm for the pump were achieved, which opened the way for very short device lengths that are vital for ultrafast pulse amplification, especially for high pulse energy and high peak power levels [45]. Moreover, a relatively much lower quantum defect of Yb allows fiber laser amplifiers with pump-to-signal efficiencies up to 90%.

2.1.2. Femtosecond Pulse Generation via Modelocking

Modelocking [46] is a group of methods to obtain ultrafast pulses from lasers. In this method, the laser resonator contains a modelocking device that can either be an active component (such as an optical modulator) or a passive element with specific nonlinear properties (such as a saturable absorber), which leads to the generation of an ultrafast pulse propagating in the laser resonator. Modelocking state is often achieved after a while and many round trips of pulses circulating in the cavity. The pulses eventually reach a steady state where a balance in the pulse parameters occur and do not change significantly variate from one round trip to the other. The duration to reach this steady state may differ according to the modelocking scheme and cavity design parameters. After reaching the steady-state, uniformly spaced pulses with equal amplitude leave the cavity through a coupler mirror, beam splitter, or fiber-based coupler to be used for different applications. Assuming that there is a single pulse circulating in the cavity in the steady-state, the pulse repetition rate of the obtained pulses is defined by the length of the cavity and the speed of light in the fiber and free-space parts of the cavity. In fiber oscillators, typical pulse repetition rates are in the range of a few MHz to 100s of MHz, which corresponds to ns time scales. In contrast, the typical pulse durations in the modelocking regime are mostly in between 30 fs to

30 ps. Hence, the obtained peak powers from the oscillator are orders of magnitude higher than the measured average power.

In solid-state lasers, the earlier mode-locking mechanisms for modelocking are using Kerr-type saturable absorbers [47, 48] and nonlinear self-focusing [49]. Further developments are achieved by using semiconductor saturable absorbers in the early 1990s [50]. In parallel to these progress in solid-state lasers, fiber lasers that can generate pulses in picosecond [51], sub-picosecond [52] and even in 100 fs range have been shown [53]. In general, passive modelocking is advantageous in obtaining the shortest pulses, and different cavity designs to obtain passive modelocking have been investigated. Early mode-locking trials were realized in Nd [52] and Er [54] based fiber lasers and by the advancement of Yb [55] and Tm [56] doped fibers, research has been shifted to these wavelengths due to their advantages as well as the different applications enabled by the emission wavelength of these fibers. As short as 28 fs pulses have been shown directly from a ring-type fiber oscillator was shown in a Yb-based fiber oscillator [57]. Recently, by using a particular type of fiber oscillator called Mamyshev oscillator, which uses a "perfect" saturable absorbing action (step-function like transmission-intensity curve), could stabilize a massive intracavity spectrum broadening and 15 fs pulses were obtained directly from this fiber oscillator [58].

When an optical pulse with high peak power propagates through a non-polarization-maintaining optical fiber, an intensity-dependent nonlinear change occurs in the polarization state by the combination of self-phase modulation, cross-phase modulation and unwanted birefringence of the fiber [53]. If the pulse that has gone through a nonlinear polarization rotation enters into a polarizer, the polarizer's output will also be power dependent. This is usually an unwanted effect in the case of fiber amplifiers. However, it also can be utilized for modelocking of the fiber laser oscillators. In order to obtain a configuration to use nonlinear polarization as a saturable absorber, fiber polarization controllers or waveplates can be implemented, so that the polarization state can be adjusted to pass the high intensity light through a polarizer and eliminate low intensity edges of the pulse and noise to shorten the pulse. Since it is based on Kerr-effect, which is very fast, the obtained saturable absorber is also fast, and the modulation output

can be adjusted with the polarization controller components. This adjustability makes the nonlinear polarization rotation a compelling technique to obtain modelock. However, the biggest disadvantage of this technique is the susceptibility to instability due to environmental factors such as temperature changes and mechanical vibrations that may affect the fiber polarization states. Hence, the repeatability of the modelock state is hard to obtain. A more environmentally robust modelocking scheme with nonlinear polarization rotation can be obtained using a polarization-maintaining fibers and Faraday rotators [59]. However, this scheme is harder to design in an all-fiber format.

Analytic solutions for the evolution of pulse during the propagation inside fiber in modelocked fiber lasers are achievable under a few assumptions [60,61]. Some of the most useful models to comprehend the laser dynamics are; soliton fiber laser model [62], dispersion management, and Gaussian pulses [53] and similariton lasers [63].

Soliton lasers generate pulses in the form of;

$$\mathbf{A}(t) = A_0 sech(t/\tau) exp(i\phi_s) \tag{2.1}$$

Here the full width at half maximum (FWHM) pulse width is $\Delta t = 1.763\tau$. In the equation 2.1, variable ϕ_s is the soliton phase and is defined as $\phi_s = |\beta_2|z/2\tau^2$, where β_2 is the group velocity dispersion of the medium. Solitons are formed using the balance of the phase perturbations caused by self-phase modulation and the dispersion and generally bandwidth limited. By neglecting the bandwidth limitation, the pulse energy (E_s) and FWHM pulse width (Δt) for a stable soliton laser can be given as;

$$E_s = \frac{3.53\sqrt{|D_2|}}{\gamma L} \tag{2.2}$$

$$\Delta t_s = \sqrt{|D_2|} \tag{2.3}$$

Here, $\gamma = 2\pi n_2/\lambda A$ is the nonlinearity parameter for the fiber where $n_2 \approx$ 2.6 x

$10^{-20}\mathrm{m}^2 \cdot W^{-1}$ is the nonlinear refractive index for silica glass. A stands for the mode area for the fundamental mode and λ is the wavelength of operation, where D_2 and L_2 are the intracavity dispersion and intracavity fiber length respectively. Utilizing high values of dispersion like chirped fiber Bragg gratings, one can obtain relatively high pulse energies and peak powers from the cavity [64]. Hence, soliton type cavities are best at obtaining picosecond pulses (due to bandwidth limitations) with energies up to 10 nJ [65].

Similarly, Gaussian-shaped pulses obtained from dispersion-managed lasers (Gaussian lasers) can be expressed in the form of $A(t) = A_0 exp[(-t/2\tau)^2]$ using the expressions below;

$$E_g = \frac{4.47\sqrt{|D_2|}}{\gamma L} \tag{2.4}$$

$$\Delta t_g = 0.66\sqrt{|D_2|} \tag{2.5}$$

Here, the governing factor affecting the pulse width is the total amount of positive dispersion inside the cavity, $D_2 = +\beta 2z$, whereas it is the average dispersion for the soliton pulse case. Hence, the generation of Gaussian pulses is possible in dispersion-managed cavities comprising lengths of both positive- and negative-dispersion fiber [66]. Differently from solitons, the Gaussian laser pulse widths variate in different positions of the cavity, and a significant pulse breathing can be observed. Hence, two points inside the cavity offer bandwidth-limited states of the pulses [66]. Like in the case of solitons, Gaussian lasers can maintain nonlinear phase delay up to . However, Gaussian pulses are generated exactly when spectral broadening due to self-phase modulation is compensated by the self-phase modulation induced pulse compression. The expressions in 2.4 are shown in [67] using numerical modeling.

2.1.3. Femtosecond Pulse Amplification

Although the modelocked oscillators generate pulses substantially higher peak powers comparing to their average power, many applications necessitate even higher pulse energies and peak powers than the oscillators can generate. Thus, post-amplification is often required. For ultrafast amplification inside the fiber, the key element is the fibers with large mode areas. Therefore, the progress of ultrafast pulse amplification has been closely related to large-core area fiber development. The first short pulse amplification experiments have been carried out in Nd- and Er-doped fibers [68–70]. In Erbium amplifiers, Raman soliton formation is further utilized for pulse compression [70], which led to the first fiber amplifier using a fiber oscillator as seed [71]. In these early systems, the maximum pulse energy was only a few nanojoules, and further amplification led to the pulse energy levels of 7.4 nJ [72].

The breakthrough in ultrafast pulse amplification has been possible through chirped pulse amplification (CPA) [73]. In this method, the pulses to be amplified are chirped and temporally broadened to a much longer durations employing a strongly dispersive element (the pulse stretcher, i.e., a long passive fiber or chirped fiber Bragg grating for fiber-based systems) and the broadened pulses go through amplification stage. Since the peak power of the pulses are reduced to a level where the detrimental effects in the fiber cause the pulses to broaden, lose their temporal and spectral shape, higher pulse energies can be deposited into the pulses during amplification. Just after the amplification, an element with an opposite dispersion (usually a grating pair) is used to remove the chirp so that the pulses return to a similar state but with much higher pulse energy compared to the input of the amplifier [74]. Compact and effective CPA systems can be constructed using chirped fiber Bragg gratings [75] or volume Bragg gratings [76] for pulse compression and stretching. Compression factors of around 1000 were achieved using simple fiber stretchers and in combination with bulk gratings [77]. However, bulk gratings and fibers usually are successful at compensating second-order dispersion, and they are incapable of compensating higher orders of dispersion. This mismatch can be compensated with special types of dispersion compensating fibers with anomalous third-order dispersion [78]. By using combinations of these stretching

and compression methods, compression ratios of up to 20000 are possible.

On the compressibility of the pulses in CPA systems, one of the limiting factors for the pulse width of the output pulses is gain narrowing. Er and Yb doped fibers have a highly non-uniform spectrum shape that is dependent on the inversion. However, the gain spectra can be calculated using the average amount of inversion and the absorption and emission spectra of the gain fiber [79]. At 1030 nm, Yb amplifiers have a gain bandwidth of around 20 nm. In contrast, the bandwidth around 1060 nm is exceeding 50 nm. These bandwidths are possible in low inversion rates. Using this range, as short as 75 fs pulses are obtained from 100 nJ pulses at a center wavelength of 1060 nm, 28 dB of amplifier gain is measured [77].

The obtainable maximum pulse energy from a CPA system is limited by the self-phase modulation, damage of fiber, self-focusing, and ratios that achievable pulse stretching and compression. For instance, a pulse stretcher and compressor with a ratio of 20000, it is possible to stretch a 100 fs pulse system to 2 ns before fiber amplifier. However, at such high compression ratios, higher-order dispersion effects in fiber should also be compensated. Grism is an alternative to be implemented in such a scenario [80]. The achievable energy that is limited only by self-phase-modulation from a CPA system can be calculated using;

$$E = \frac{B\tau}{\gamma L_{eff}} \tag{2.6}$$

where τ is the pulse width of the stretched pulses, L_{eff} is the effective amplifier length, γ is the nonlinear coefficient and given as $\gamma = 2\pi n_2/\lambda A_{eff}$, and n_2 is the nonlinear refractive index at wavelength λ. For high-gain amplifiers (G $>$ 10 dB), the sufficient amplifier length is given by $L_{eff} \approx 4.34 L_{amp}/G$, where G is the total gain of the amplifier in decibels. Here B is an integral (B-integral) defined as;

$$B = \frac{2\pi}{\lambda} \int n_2 I(z) dz \tag{2.7}$$

where $I(z)$ is the optical intensity along the beam axis, z is the position in beam direction and n2 the nonlinear index quantifying the Kerr nonlinearity [74]. Since $n_2 I$ is the nonlinear change in the refractive index, the B integral gives the cumulative on-axis nonlinear phase shift during the passage through the fiber. Hence, assuming a stretched pulse width of $\tau = 2$ ns, an effective amplifier length $L_{eff} = 0.25$ m, $\gamma \approx 4 \times 10^{-5}$ (m·W)$^{-1}$ (for a mode area of 4000 μm^2), and a B-integral of 10, we obtain a maximum possible pulse energy of 2 mJ, which is close to the experimental limitations of ultrafast fiber laser amplification.

At such high pulse energies, Raman scattering, self-focusing, and optical damage to the fiber define the maximum allowable peak powers in the fiber amplifier and the maximum obtainable pulse energy. In optical fibers, the self-focusing limit is believed to be around ≈ 6 MW [81] of peak power, which corresponds to a pulse energy of ≈ 10 mJ for stretched pulses around 2 ns in pulse duration. Raman scattering related pulse energy limitation in optical fibers given by $E_r = 16A\tau/\gamma r L_{eff}$ ($\gamma r = 1 \times 10^{-13}$ m/W is the peak Raman gain coefficient) and is estimated to be as $E_r = 5$ mJ. Since the current widely used host material of fiber is silica glass, the bulk energy damage threshold in optical fibers can be calculated using the fused silica's damage threshold. E_d gives it $\approx \gamma_d A\sqrt{t}$ [82], where $\gamma_d \approx 6 \times 10^{10}$ W·m^{-2}·s$^{0.5}$ and is calculated as $E_d \approx 10$ mJ. Using special polishing techniques and keeping the fiber end surfaces in a vacuumed environment, there is nearly no difference between bulk and surface damage [83].

2.2. Femtosecond Fiber Laser Simulations and Experimental Setup

The laser system built is consisted of four parts: oscillator, two preamplifiers with an acousto-optic modulator in between for repetition rate control, a high power amplifier and a compressor for pulse compression.

2.2.1. Oscillator

The schematic of the oscillator is given in Figure 2.1. The cavity consists of $\sim$ 50 cm Yb doped fiber (Yb-214), $\sim$ 315 cm single-mode passive fiber (HI-1060) and

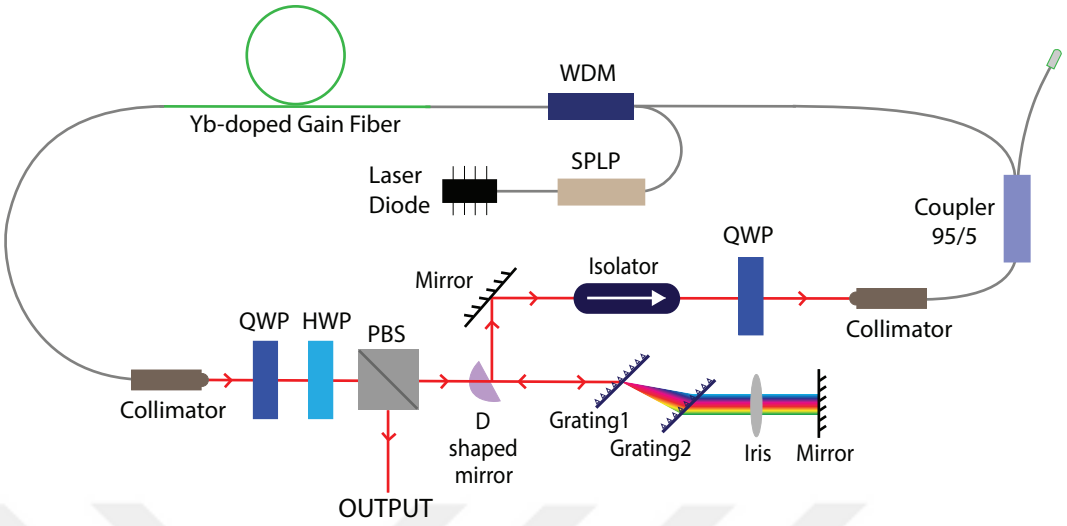

Figure 2.1. Fiber laser oscillator that is generating femtosecond pulses.

free space optical elements. Yb-doped fiber is pumped at 976 nm by a laser diode that is capable of supplying as much as 500 mW of power. A pump laser protector (SPLP) is used to prevent the light from the diode and the rotating light in the loop to be reflected to the diode. A 980/1030 nm WDM is used to combine the output of the laser diode pump and the signal. A 1030 nm wavelength is obtained from the output of the Yb doped fiber pumped by a laser diode with a wavelength of 976 nm, and the free space portion is provided by the collimator. In the free space section, a half-wave plate (HWP) that changes the polarization direction of a linear polarized light, two quarter-wave plates (QWP) that convert circular polarized light into linear polarized light, one cube (PBS) that throws the vertical polarized light out of the loop, one insulator, one pair of diffraction gratings and one filter to compensate for the group-velocity distribution (GVD) of the fibers in the loop are used. The cavity design is dispersion managed ring-type oscillator. There were a few reasons to choose this type of cavity and the repetition rate. The most important ones are obtaining pulses as short as possible from the oscillator while maintaining the stability and reducing the complexity. Since our application field was transparent material processing, it is important to obtain pulses as short as possible (ideally less than 300 fs). The other important factor is the stability. Since we are aiming to investigate a parameter space and optimize the system according to the glass welding experiments, it is important to obtain self-starting and long-term stable modelock, especially during the experiments.

According to these criteria we have optimized the cavity design using simulations and experiments.

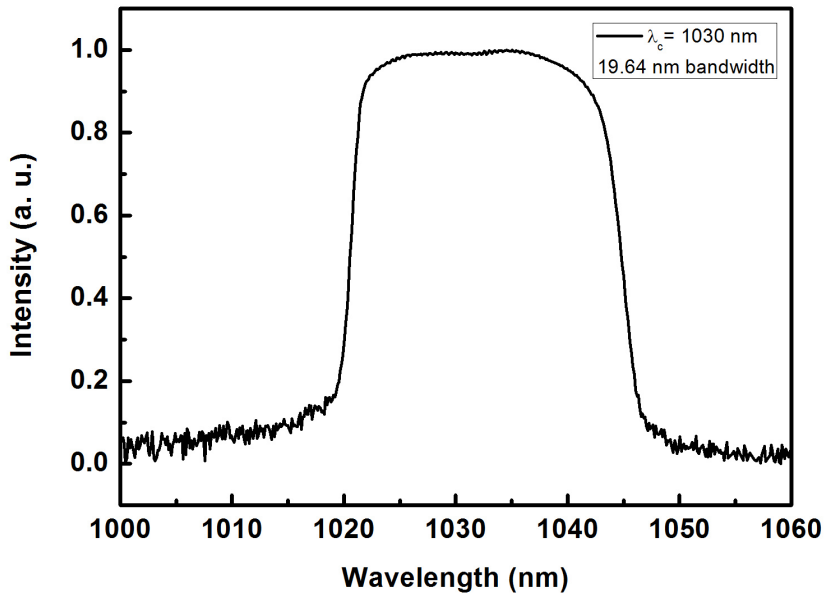

Figure 2.2. The spectrum trace of the oscillator from fiber coupler.

Stable pulses are obtained by nonlinear polarization evolution (NPE) which is achieved by the polarizing beam splitter cube and wave plates that change the polarization state of the signal. When the laser is turned on, mode-locked operation is achieved by adjusting polarization using the wave plates after the fibers in the loop were fixed. In this step, power and spectral information is monitored from the 5% output of the coupler in the loop using an optical spectrum analyzer and an optical power meter. The repetition frequency of the oscillator is determined as 50.19 MHz with the total length of the fibers used and free-space length. The distance between the refraction gratings is adjusted to compensate for the group-velocity distribution of the total fiber used. Total fiber length of the oscillator is 357 cm and free space part is 53.7 cm with a grating pair separated by a distance of 5.3 cm. Total group velocity dispersion caused by the fiber is calculated to be 88552 fs^2/mm, and total group velocity dispersion caused by grating pair is -85849fs^2/mm. In this case, net group velocity dispersion, GVD_{net}, of the oscillator is calculated to be around 2703 fs^2/mm.

Fiber output coupler in the cavity is used for diagnostic purposes. The power measured from the fiber output coupler and the output from the PBS are 0.830 mW and 52 mW, which corresponds to 0.016 nJ and 1.03 nJ respectively. Spectrum and pulse repetition rate at the output of the oscillator are given in Figure 2.2, Figure 2.2 and 2.4. Spectrum on the left is taken from the output coupler which was left for diagnostic purposes and the one on the right is taken from the output of the PBS. The pulse train generated from the oscillator has also been examined in the RF spectrum. By the combination of the oscilloscope data and the RF spectrum data, single pulse operation of the oscillator is verified. The RF data showing the fundamental frequency ($\approx$ 50.19 MHz) can be seen in Figure 2.5.

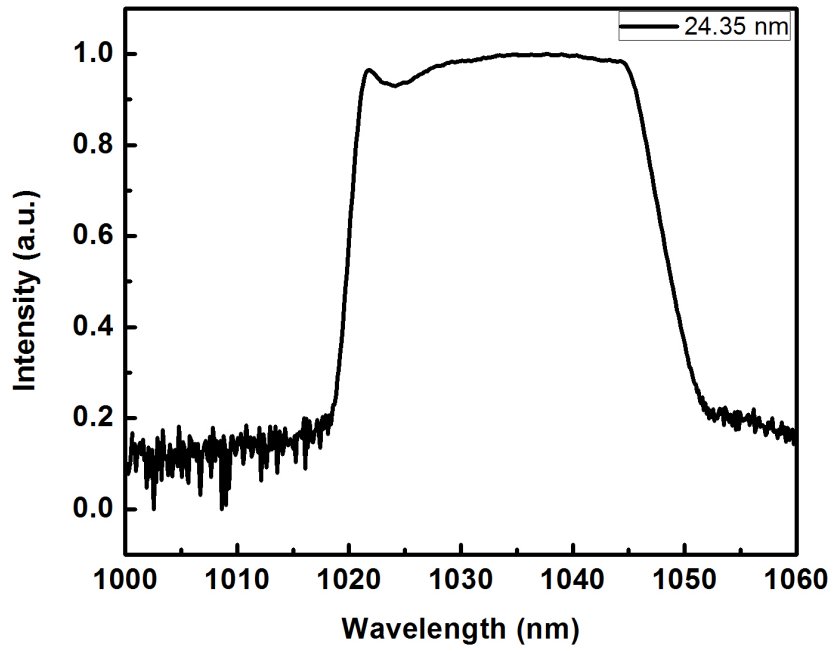

Figure 2.3. The spectrum trace of the oscillator from PBS output.

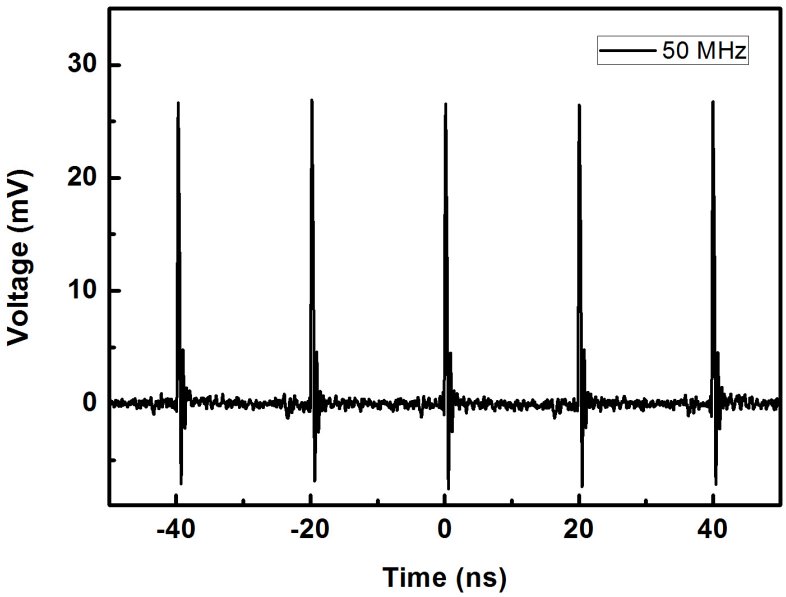

Figure 2.4. The pulse train at 50.19 MHz generated from the oscillator.

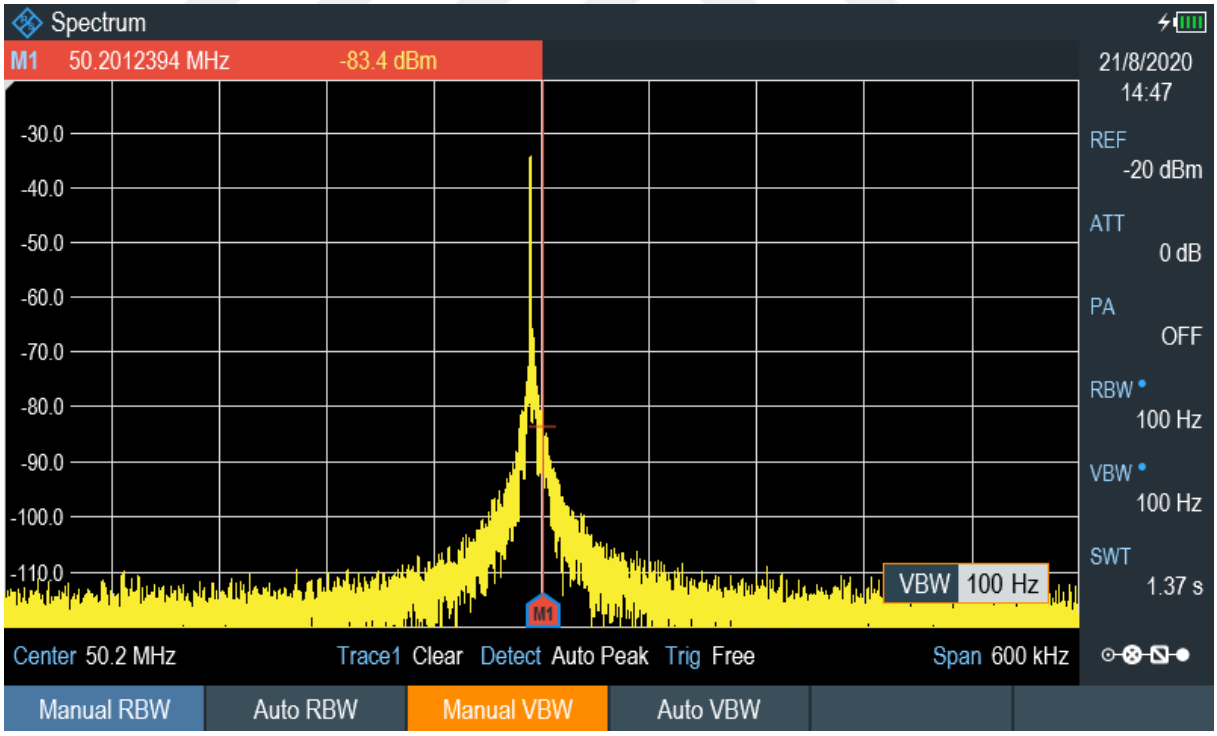

Figure 2.5. RF spectrum analyzer data of the pulse train generated by the oscillator.

2.2.2. Preamplifiers and High Power Amplifier Simulations

Before building preamplifiers and high power amplifier, we simulated the evolution of pulses with a program that simulates nonlinear pulse propagation. We made

the simulations in a way to reach the highest pulse energy, the shortest pulse duration and therefore the highest peak power using minimum amplifier stage and simple components. The fiber lengths we have used were revised and adjusted according to the simulation results. Compared to going purely experimental, this saved us time.

The simulation we used is a pulse propagator simulation used to simulate fiber lasers and fiber amplifiers developed by UFOLAB, Bilkent University. For given inputs, it solves Generalized Nonlinear Schrödinger Equation (GNLSE) using split step fourier method. It includes the effects of second-order dispersion, third-order dispersion, loss and gain, Kerr nonlinearity, self-steepening and simplified Raman scattering.

Table 2.1. Parameters used in simulation.

General Parameters	Initial pulse shape	Initial pulse width	Initial peak power
	Time window length	Total number of passes	Save every N, pass N
	Central wavelength	Number of integration steps	
Segment Parameters	**Fiber**		
	Dispersion Parameters	**Nonlinearity Parameters**	**Gain-Loss Parameters**
	GVD	Kerr coefficient	Passive/Active fiber
	TOD	Effective mode area	Central wavelength of the gain
		Raman response	Gain bandwitdh
		Fiber length	Effective gain saturation energy
	Other		
	Saturable Absorber	**Bandpass Filter**	
	S.A. type	Filter type	
	S.A. parameters	Central wavelength	
		FWHM bandwidth	

The simulation was performed separately for each part of the laser by entering the laser parameters listed in Table 2. According to the results, duration of the shortest pulse with a pulse energy of 5 μJ is 217 fs, the bandwidth of the spectrum is 14 nm.

2.2.3. Preamplifiers and High Power Amplifier

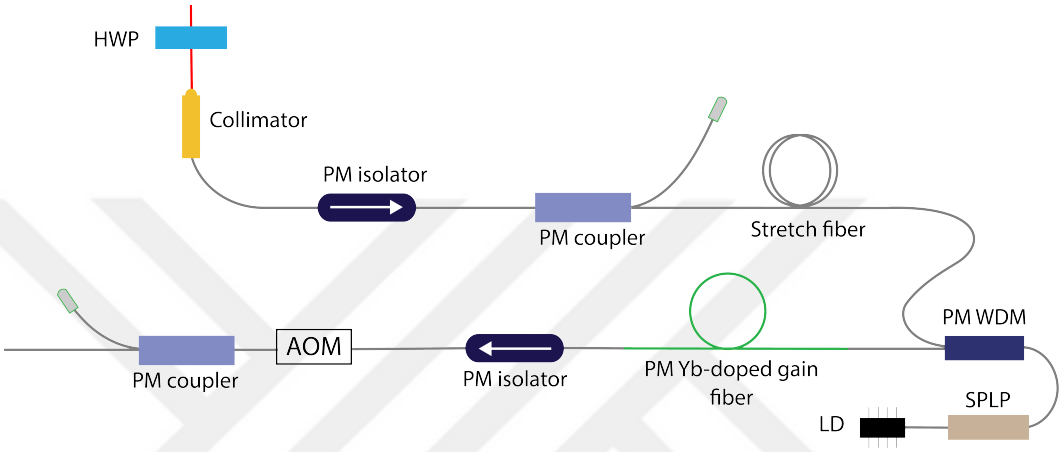

Figure 2.6. The scheme of the first preamplifier.

The output of the polarizing beam splitter cube is coupled to a polarizing maintaining fiber using a collimator. The light coming out of the cube has vertical polarization. We can change the polarization angle by using a half wave plate and thus we can adjust the amount at the isolator output we placed after the collimator. All fiber components beyond this point are polarization maintaining. Before the first preamplifier stage, an isolator and an output coupler are placed to prevent back-reflections and for diagnostic purposes, respectively. In order to compensate for the nonlinear effects to be increased in the amplifier steps, passive fibers of $\sim$ 100 m length is used before the first preamplifier and the width of the pulses is increased from $\sim$ 3 ps to $\sim$ 50 ps. At this point, the average optical power is measured to be 18 mW and the corresponding pulse energy is calculated to be 0.36 nJ.

At the first preamplifier stage, shown in Figure 2.6, a laser diode delivering a maximum power of 500 mW is used as a pump source. A laser pump protector is used to protect the diode laser from possible back reflections. A WDM is used to combine the signal and the pump so that they can propagate simultaneously through the Yb-doped gain fiber. Following the Yb-doped fiber an isolator is used to protect

this preamplifier stage from possible back-reflections. The length of Yb-doped fiber (PM Yb-401) is 0.6 m. The average optical power of the amplified signal is $\sim$ 300 mW, pulse repetition frequency is 50.19 MHz, and pulse energy is $\sim$ 6 nJ. Figure 2.7 and Figure 2.8 show the optical spectrum taken from the output of first the preamplifier stage before and after the amplification. Keeping the signal remained the same, the preamplifier stage was characterized by measuring the output power and obtaining the output spectrum while increasing pump power with constant current values. As shown in the Figure 2.9, the level of signal increases for increased pump power and bandwidth of the spectrum decreases due to the gain narrowing effect.

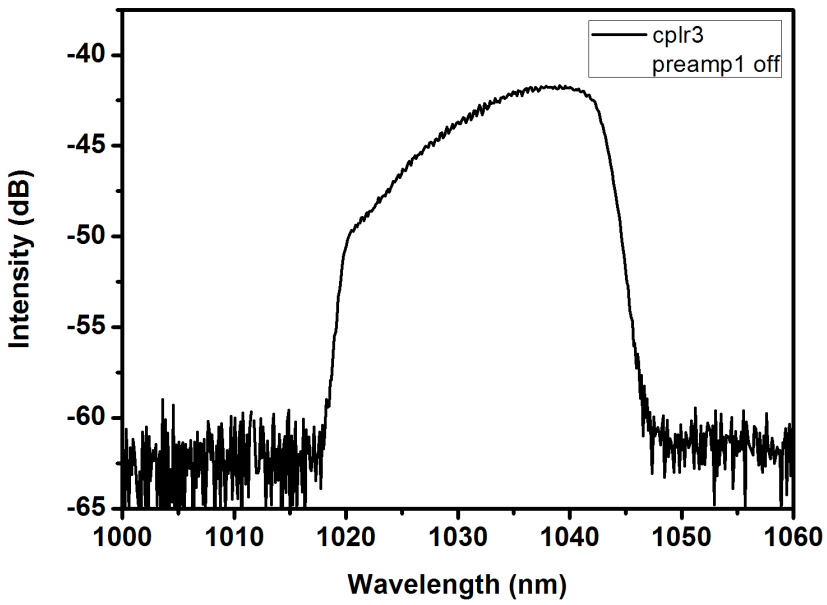

Figure 2.7. The spectrum of the preamplifier before the amplification.

To control the pulse repetition frequency of laser pulses, fiber integrated acusto-optic modulator (AOM) controlled by a field-programmable gate array (FPGA) is placed between the two preamplifier stages. AOM reduces the pulse repetition frequency for amplification to high power levels. Internal loss of AOM is around 50%. Average optical power of the output is around 150 mW and calculated pulse energy is $\sim$ 3 nJ for 400 kHz repetition frequency.

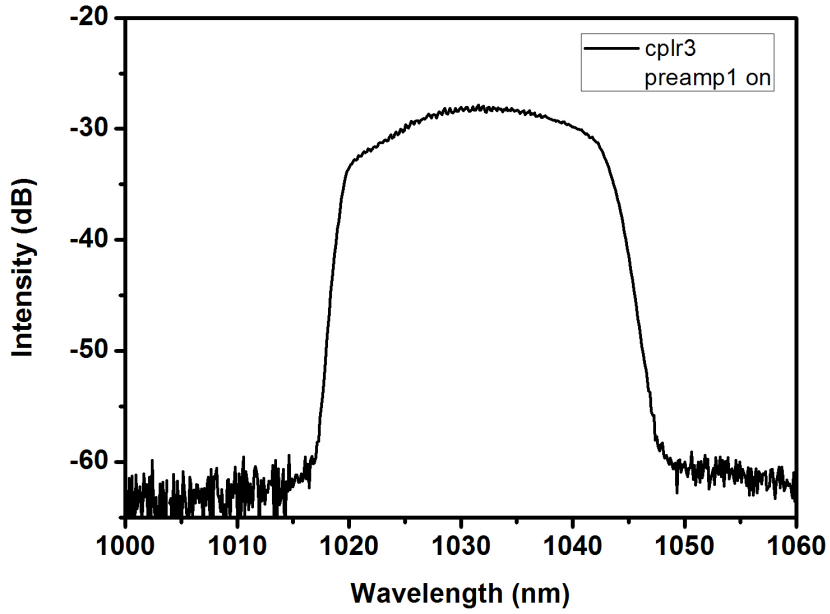

Figure 2.8. The spectrum of the preamplifier after the amplification.

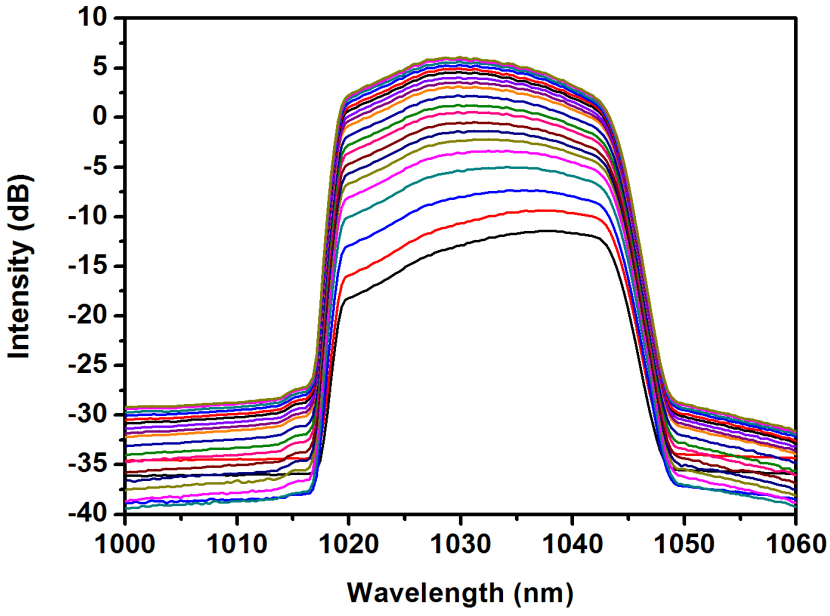

Figure 2.9. Optical spectrum trace of the first preamplifier with varying diode current for constant input signal.

Following the AOM, a second preamplifier which is exactly the same as the first one is built to compensate the losses caused by the internal lossof the AOM and the reduced repetition frequency. The length of the Yb-doped gain fiber (Yb-401) used is

0.6 m. Using this second preamplifier, the signal level is increased to 26 mW power which corresponds to $\sim$ 65 nJ energy. Figure 2.10 and Figure 2.11 show the schematics of the second preamplifier and the same characterization result that we did for the first preamplifier correspondingly.

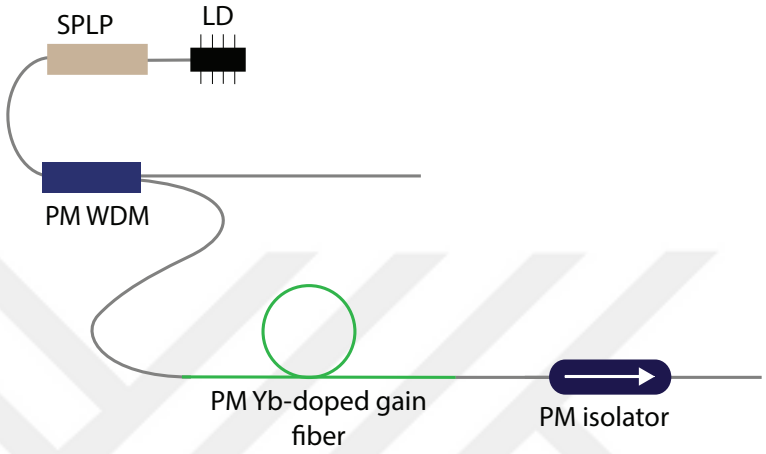

Figure 2.10. Schematic of the second preamplifier of the fs fiber laser.

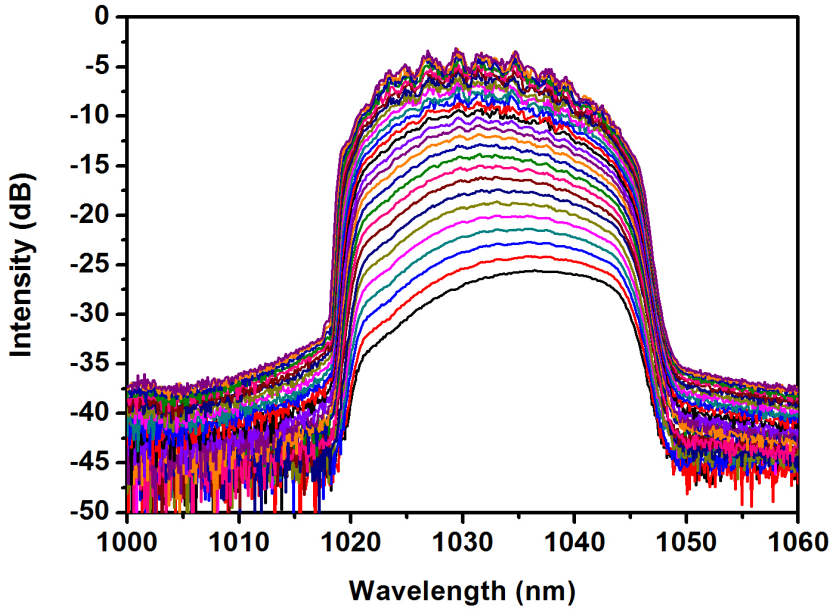

Figure 2.11. The spectrum trace of the second preamplifier output with varying laser diode current.

At the end of the preamplifiers, MPC (multi-mode pump combiner) is used to combine the pump at a wavelength of 976 nm with a maximum power of 18 W and the signal coming from the pre-amplifier stages. A 1 meter long double clad Yb-doped

fiber (Yb1200-20/125DC-PM) with a compatible core diameter with MPC fiber is used to handle the high optical power of signal and the pump. The pump diode used in this stage is temperature-stabilized to avoid the shifting of the diode output wavelength with a change in temperature. Since Yb-doped fibers have a peak for absorption around 976 nm wavelength, any shift that may occur causes a decrease at the absorption rate of the pump power. This, consequently results in efficiency drop in amplification process. This may even cause the burning of the fiber or components in the amplifier because the unabsorbed pump power may reach to high enough levels. The average optical power of the amplified at this stage is $\sim 5.5\ \mu$J.

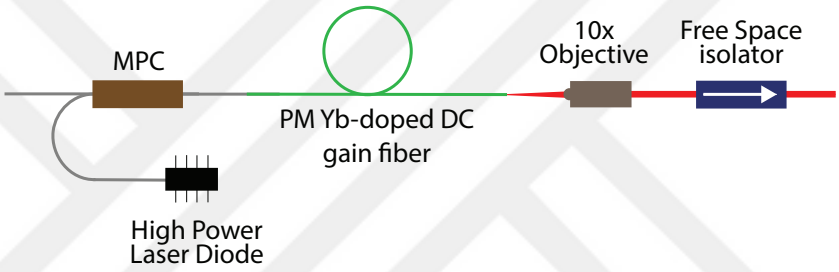

Figure 2.12. The scheme of the power amplifier of the fs fiber laser setup.

Light output from the double clad Yb-doped gain fiber is collimated using a 10x high power objective. The tip of this fiber is cleaved at an angle of 7 degrees to prevent back reflections from the cleaved surface. If the tip was cut straight, there would be 8% back reflection from the fiber end. A high power free-space isolator which can withstand up to 40 W optical power is placed to prevent back reflections from the target and the optical elements, as well. One half-wave plate (HWP) and polarizing beam splitter cube (PBS) are placed to adjust the output power. Following the HWP and PBS, a pair of diffraction gratings with 1200 line/mm are used to compress the resulting pulses. In order to set the grating separation where the output pulses are the shortest, intensity autocorrelation technique is used, the grating separation where we obtained the shortest pulse was approximately 30 cm. The width of the compressed pulses is $\sim$ 250 fs, which is very close to the simulation result and the maximum pulse energy is $\sim 5\ \mu$J. Grating efficiency approximately 85% Figure 2.13 and Figure 2.14 show the optical spectrum and the autocorrelation trace of the pulse after the compression.

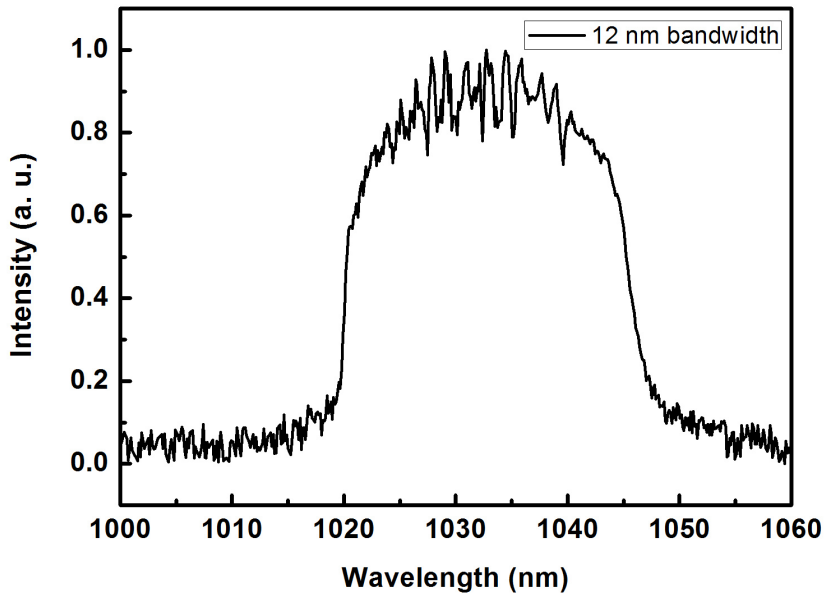

Figure 2.13. The compressor output spectrum.

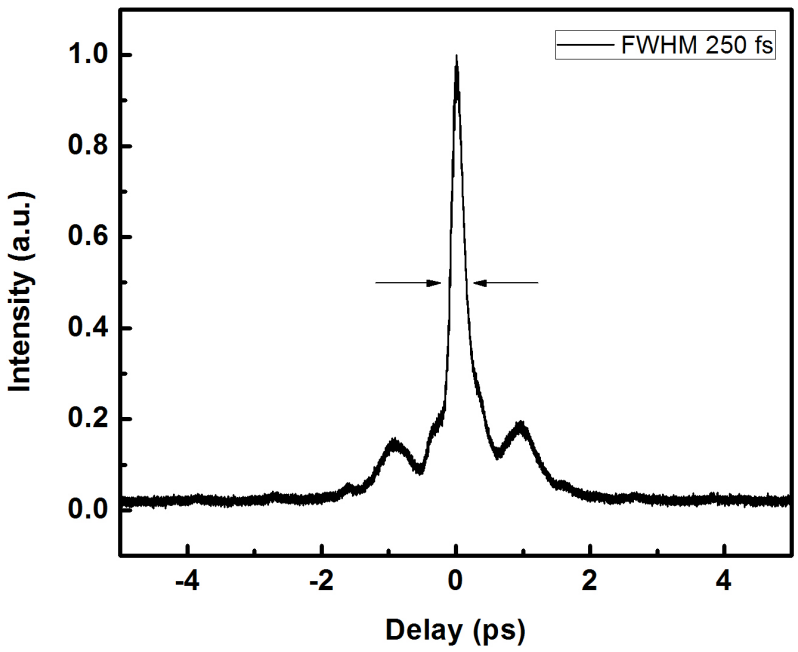

Figure 2.14. The compressor output autocorrelation trace.

Power characterization of the high power amplifier stage is done by measuring the output of the amplified signal as a function of pump power of the high power amplifier. By placing a longpass filter (FEL1000, Thorlabs Inc.) which transmits the

signal wavelength and reflects the pump, amplified signal is measured while increasing the current of diode driver with 200 mA steps. Measured values are corrected taking into account the loss of the filter and plotted against the pump power corresponding to the current of diode driver.According to the measured output powers and corresponding applied pump powers, a conversion efficiency of 65% is achieved.

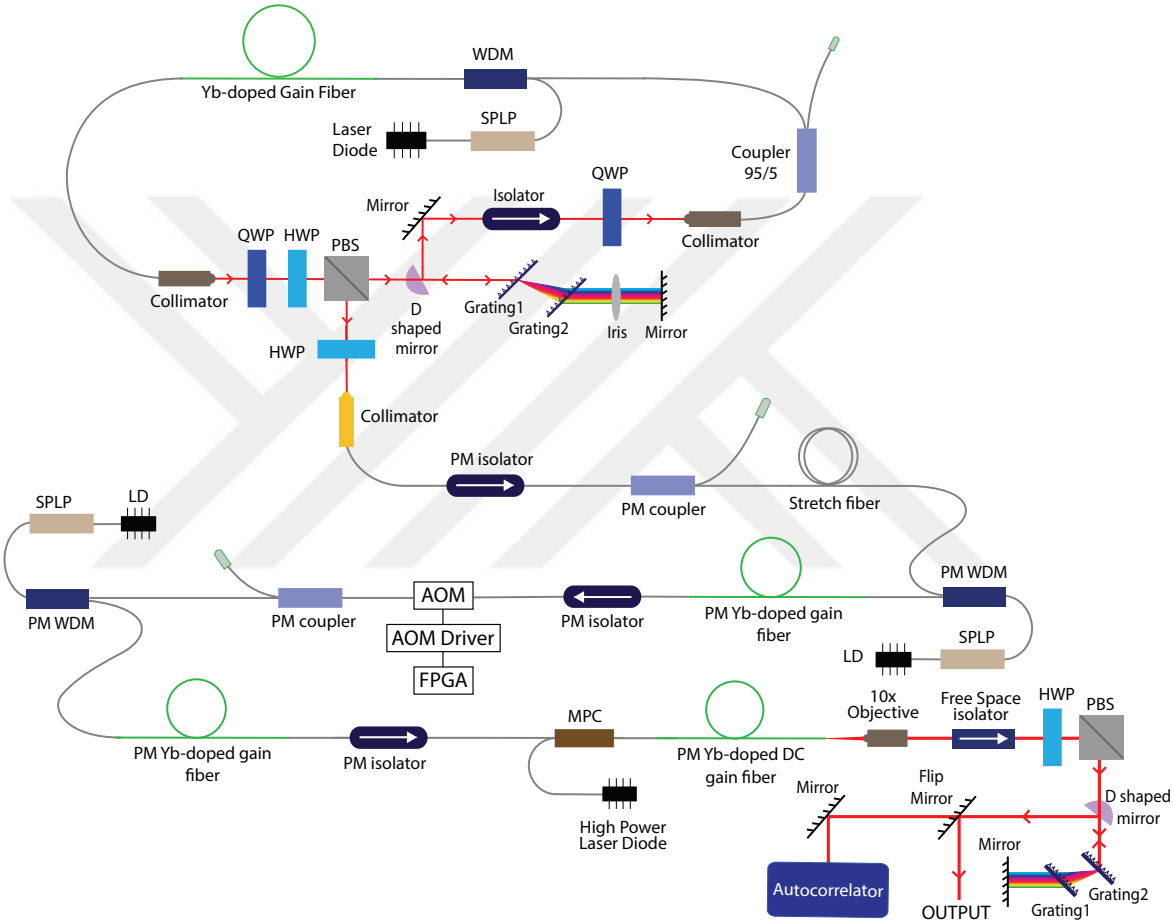

Figure 2.15. Complete setup scheme for the fs fiber laser. The laser consists of four parts: oscillator, two preamplifiers with an acousto-optic modulator in between for repetition rate control, a high power amplifier and a compressor for pulse compression.

Other characterizations made on the system were long-term position stability measurement and long-term optical power stability measurement from the output beam of the compressor. For long-term power measurement, we placed the power meter sensor on the compressor output, turned on the laser and recorded a 5-hour measurement. Figure 2.16 shows the recorded data together with the std% calculation. For long-term position stability measurement, we placed a CCD camera on the compressor output and recorded an image every 10 minutes. For each recorded image, we found the pixel corresponding to the midpoint of the beam and plotted the change of the position over time. Figure 2.17 shows the displacement of the beam center in x and y coordinates. According to this measurement, the std calculated in the x and y axes was 3.1 μm for the x axis and 5.4 μm for the y axis. Taking into account the path of light from the output of the objective, beam pointing stability was calculated to be 104 μrad.

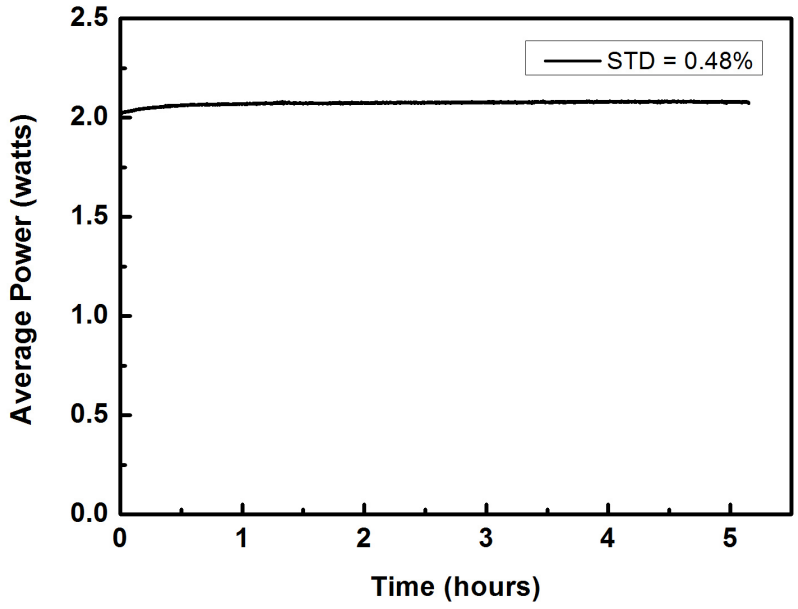

Figure 2.16. Long term optical power stability measurements from the output of the compressor.

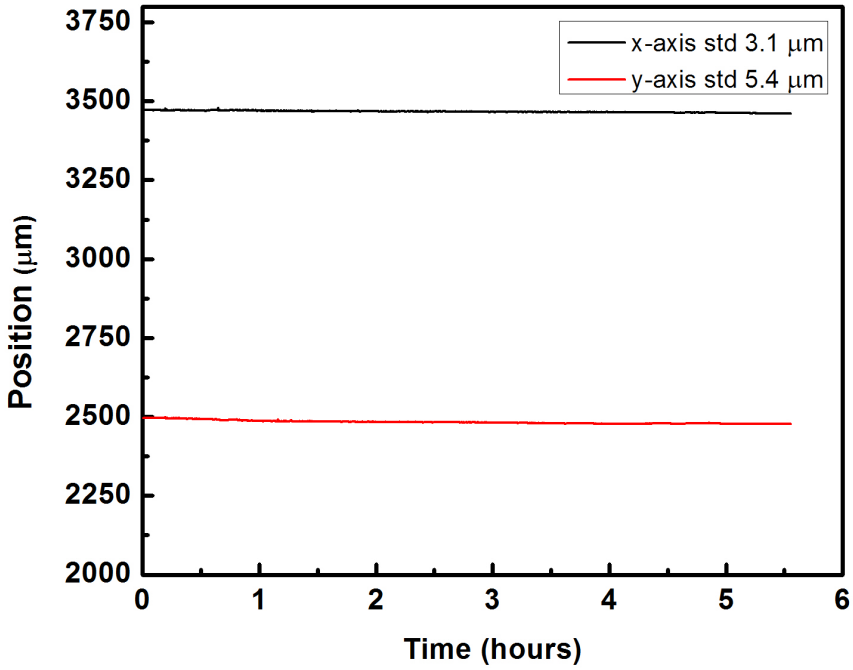

Figure 2.17. Long term beam position stability measurement from the output of the compressor.

2.2.4. Electronic Control of the Laser Setup

To control the custom-developed fiber laser setup, we have also developed a flexible control electronics scheme similar to the setup in [84]. We used an FPGA based control circuit and control all of the stages of the laser setup using the same board. The FPGA is getting its trigger signal from the oscillator pulse train from one of the output ports using a photodiode and RF electronics that provides voltage level compatibility for triggering between the oscillator output and the FPGA input. Using this scheme, all the system is inherently synchronized to the fundamental laser frequency. There are two types of laser diodes in the setup. One of them is single-mode low current (<1A) laser diodes that are used to pump single-mode stages such as oscillator and preamplifier. The other type is high current ($\approx$ 10A) diodes that are pumping the amplifier stage. Single-mode and high power diodes are driven using different driver modules capable of giving different current levels. However, all of the diode drivers' current levels are controlled via analog inputs from a digital to analog converters (DAC)

controlled by the FPGA. Hence, the diode current levels can be adjusted quickly and independently from the FPGA program. Besides, single-mode diodes necessitate to be in constant temperature, and they have internal TEC (thermoelectric cooler) modules. These modules are also driven by TEC control circuits and kept at constant temperature (around 30°C) for safe operation. The same FPGA circuit is utilized to handle pulse picking. Pulse picking is realized using an acousto optic modulator (AOM) positioned after the first preamplifier stage. AOM is driven with a high-voltage (30 V_{pp}) RF driver with a carrier frequency of 200 MHz. Gating signals formed by the FPGA are used to modulate the RF driver so that a pulse envelope is formed and applied to the AOM, such that single pulses are transmitted in selected periods. The repetition rate is chosen via buttons on the FPGA circuit. Currently, repetition rates between 100 kHz and 400 kHz can be applied to the AOM using this scheme. For the synchronization of the pulse picking scheme with the laser system, a signal directly from the oscillator is taken via a fast photodiode. The output is fed to the FPGA as the clock source. To obtain high temporal resolution to adjust the delay and the gate signal, a faster clock signal is needed. Thus, the clock signal derived from the laser's repetition rate is multiplied by four at the digital clock manager inside the FPGA to 200MHz, which is providing us 5 ns resolution in adjusting the delay and gate signals.

In addition to pulse picking and diode driving tasks, the laser's stages are also enabled by the same FPGA card. By using the diagnostic ports positioned after every stage, we have formed feedback setups such that every section of the laser setup is turned on only after the previous stages are operating correctly. Suppose the system has a problem in one of the stages. In that case, all the succeeding stages are disabled by the FPGA with pre-defined delays such that the amplified spontaneous emission or giant pulses that may damage the components are not formed in the amplifier system in the lack of signal.

3. FEMTOSECOND LASER GLASS WELDING

3.1. Introduction

Since the advent of ultra-short pulsed lasers with both adequately high pulse energy and pulse repetition rate, over the last decade an additional glass joining mechanism has become usable. This new technique, glass welding by ultra-short lasers, it offers short processing times, does not require additional materials and benefits fusion welding of glass components.

In 2005, Tamaki et al published a first overview of ultrashort-pulsed laser glass welding of silica glasses [28]. At the time, laser parameters Tamaki et al used for glass welding were 1 μJ pulses with a pulse length of FWHM 130 fs at 800 nm with a repetition rate of 1 kHz. They achieved optical contact before the welding process and irradiated the sample by scanning two dimensionlly in the xy-plane with a translation speed of 5 μm/s. Next year, the same group also managed to weld non-alkali alumino silicate glass substrates using 1558 nm laser pulses with pulse duration of 947 fs and repetition rate at 500 kHz [85]. They took also strength measurements of their welded samples and reported a joing strength of 9.87 MPa. Although far higher translation speeds and repetition rates are usually used today, those parameters may have been attributed to the lack of high repetition and high energy ultrashort-pulsed laser sources available.

In the following years, many computational studies were conducted to understand the interaction of ultrafast lasers with transparent materials. In 2007, Miyamoto et al [86]reported the local melting of glasses by calculating spatial and temporal distributions of the temperature inside the material and commented on crack-free melting. Okamoto et al [29] developed a computational model using transient thermal conduction model to see the dependency of the time between the pulses on temperature. They also analyzed crack-free conditions in heating and cooling processes based on the simple thermal stress model. They found out that cracks can be prevented for some cases.

One case when the incoming laser pulse hits the glass with a temperature higher than the softening temperature of the glass, second case is when there is a dual-structure having a teardrop shape and an outer molten structure. Same group developed another model which can be applicable to successive laser pulses with high repetition rates to evaluate the distribution of the laser energy absorbed in bulk glass [87].

Up to 2015, published welding researches had implemented methods to reduce the gap between the two glasses before irradiation. Possible approaches were employing clamping mechanism to press the samples together from the edges, an additional lens to press the substrates at an extra point, etc. These techniques were useful reducing the gap size to prevent crack formation, however as soon as the clamping device is removed, sampled were experiencing an excess stress because of bending. Optical contacting could bypass these issues however for industrial applications, it was not a practical and automated method.

Gap bridging methods for ultrashort-pulsed laser glass welding therefore caught the researchers' attention and were carefully investigated. In 2015, the first successive gap bridging results were published by Cvecek et al [31], Chen et al [21] and Richter et al [88]. Cvecek et al [31] conducted experiments to confirm the idea the adjacent parts of the plasma become viscous due to the temperature distribution so that the surface bulges out irreversibly without any crack formation. They also suggested that to prevent uncontrolled melt relaxation into the gap, the surface temperature should be low enough to cause sufficiently high surface tension. The process was explained as follows; in case the bulge forming inside the first plate covers a distance to a second glass plate, van der Waals forces provides initial direct contact if they got close enough to each other. Meanwhile, heat conduction causes a softening of the surface of the other glass plate. The shrinking of the molten pool during cooldown gets closer both plates to each other through van der Waals forces. Therefore, the slightly decreased distance can support a subsequent welding seam at a new location and thereby have better bonding and a greater distance reduction. Also molecular diffusion may be feasible at any stage, because the bonding energies found grater than the bonding energy of pure van der Waals bonding. In this way, gap between glasses becomes closed. Cvecek et al

achieved successful gap bridging results using soda-lime, Borofloat33, D263 borosilicate glass and fused-silica. Maximum gap they could weld was 1 μm with laser parameters of 2 μJ pulse energy, 1 MHz repetition rate and 10 ps pulse duration.

Chen et al [21] conducted experiments which investigates effect of the focal spot position and pulse energy on gap bridging. Their findings showed that the melt pool should be centered on approximately one plate so that a wider range of the processing parameter would be available. They also demonstrated that bridging occurs with large pulse energies, even though the melt pool is focused between the glass plates. They could weld two glasses with 3 μm gap using a pulse energy of 18.4 μJ, repetition rate of 400 kHz and pulse duration of 5.9 ps. They found a linear dependency between the pulse energy and the bridgeable gap size. According to their findings, idea of the Cvecek et al found missing since the melt relaxation could be prevented by having a centrally positioned large melt pool. Nonetheless, these findings indicated that there is an upper limit to the crack-free bridgeable gap scale, because cracks could develop across the melt pool while resolidification [89].

Richter et al [88] showed the effects of bursts of four pulses on gap bridging. They could weld fused-silica glass plates with 3 μm gap. 10 μJ pulses were separated temporarily by 20 ns inside bursts. Pulse duration was 500 fs and burst period was 200 kHz. They examined the size of laser induced modifications by conducting experiments with bursts consisting of 1, 2, and 4 pulses. They also investigated the effect of the distance of the focus from the surface on the amount of bulging. In terms of absorbed laser power, their experiments were similar to the studies Chen et al done, they confirmed the findings with a higher repetition rate.

More recently, a new gap bridging method of soda-lime glass plates has demonstrated [90] using a galvo scanner. Pulse energy was 12 μJ, pulse duration was 10 ps and repetition rate was 1 MHz. They created concentrically hatched circles with a 20 μm spot diameter at the interface. Circular patterns were inscripted 150 times with a scanning speed of 1 m/s. The resulting molten area was very big that it was able to reduce the gap down to 3 μm. By using this method, they could achieved a maximum

joint strength of 64 MPa. They also reported that they had cracks inside the welded area and attributed the reason to the fact that soda-lime glass has a very high thermal expansion coefficient. As a second reason, they suggested the large molten pool formed due to a relatively low NA lens.

Glass welding via ultrashort-pulsed lasers has been demonstrated to be able to combine several types of glasses such as soda-lime [90], borosilicate glasses [31], D263 [29], N-BK7 [91], fused-silica [28] and Foturan [92] . Many research groups also studied on welding of different types of glasses. Combinations of N-BK7 to Borofloat33 [21], fused-silica to borosilicate HOYA NA35 [93], fused-silica to BK7 [94], and with many other types of glasses were proved to be welded using ultrashort-pulsed lasers.

Although studies on welding of same glass and various types of glasses have been mentioned so far, joining of dissimilar materials is also necessary for many applications. Because current techniques which hold dissimilar materials together such as adhesives are short-lived and combining process is messy. Traditionally, the ultrashort-pulsed laser welding of glasses with those strongly dissimilar materials have some challenges due to their different chemical and physical properties. On the other hand, for certain situations, using different type of materials may ease the required restrictions for the process. For example, in the case of silicon to glass or metal to glass welding where silicon or metal often behaves as a good absorber and thus high numerical aperture focusing may not be needed.

There has been a persistently growing number of studies on ultrashort-pulsed laser joining of glass to dissimilar materials. For example, glass to aluminum [95], glass to sapphire [95], glass to copper [96], silicon carbide [97] and glass to steel [95] are few published examples in the literature. The ability to join glasses to other materials such as metals, silicon, ceramics, etc is an increasingly important for technology that include the development of optical sensors, actuators, encapsulation of electronic components in the manufacturing of MEMS and 'lab-on-a-chip' systems [98, 99].

3.2. Theoretical Background

3.2 displays a schematic description of the ultrashort-pulsed laser welding of glass pieces. The lasers chosen for the glass welding have a wavelength which the glass is transparent, meaning the glass has no absorption in that wavelength range. Focusing objective typically has a high numerical aperture objective. The sample is either moved with respect to the focus point of the laser or a scanning system is used to deflect the laser beam on the sample.

In ultrashort-pulsed laser glass welding, the energy input is supplied via nonlinear absorption [100, 101] if the intensity reaches up to sufficient values. According to the properties of focusing optics, and laser parameters such as pulse duration, self-focusing effects may have an effect on the shape of the focus point where the free electrons are generated [102]. There are two mechanisms for obtaining free electrons: multi-photon absorption and field ionization [103]. When multiple photons are absorbed simultaneously by one electron, multi-photon absorption occurs. If the sum of the photon energy is greater than the band gap, an electron in the conduction band is generated [82, 104]. In case of the field ionization, coulomb potential of the atom is distorted by the strong laser field, and electrons may tunnel through the potential barrier [82, 104].

Additionally, an electron already in the conduction band can absorb multiple photons and it can eventually have an energy more than the energy of the conduction band by an amount of band gap energy. Via impact ionization, an electron from the valence band may be lifted to the conduction band, while the electron that was already excited returns to the lower level at the conduction band. This results in two excited electrons near the minimum of the conduction band. Both electrons may repeat this process to induce an avalanche of excited electrons [82, 103]. The multi-photon ionization can also occur together with the avalanche ionization if the pulse duration is long enough due to the time required for the collisions [105]. Therefore, the presence of the avalanche ionization can further increase the density of the free electrons and the absorptivity of the region irradiated to cause modifications in the material , [82, 104].

For the case that the nonlinear absorption is caused by the fs laser irradiation, absorption occurs on a time scale much shorter than the time required for the energy transfer between the electrons and the lattice. This results in a non-equilibrium state which excited electrons become surrounded by a cold lattice. The density of the electrons grows until the plasma frequency P is approaches the laser frequency ω_P [82]. The plasma frequency ω_P is defined as follows

$$\omega_P = \sqrt{\frac{e^2 N}{\epsilon_0 m_e}} \tag{3.1}$$

where e denotes the elementary charge, N is the electron density in the conduction band, ϵ_0 is the electric permittivity of the free space, and m_e the mass of an electron.

When $\omega_P = \omega_P$, plasma becomes strongly absorbing and the material deposits significant fraction of the laser pulse energy. The excited electrons thermalize with the ions after absorption, and induce structural changes. Depending on the degree of the excitation refractive index changes, cracking, void formation or localized melting takes place [26, 106, 107].

Because of the high absorptivity of the plasma, ionization can occur above the focus point as well. Even at temperatures as low as a few hundred °C, free electrons generated by the thermal ionization can add up to the avalanche ionization process [31]. But the temperature decreases as we go up along the focus point. This phenomena was explained by the fact that laser energy is further absorbed by the plasma and demonstrated via some experiments and simulations [108, 109]. The fact that plasma absorbs most of the laser energy and partially shields it is the reason for the tear drop shape of the laser induced modifications as well. Nonetheless, the exact form of the melting pool is affected by the parameters such as numerical aperture, translation speed, average laser power, heat conductivity and melting point of the glass.

3.3. Experimental Setup

Figure 3.1 shows the experimental setup for the laser welding. Experiments are performed using the custom developed fiber laser system which is described in the previous section. The beam from the laser system is magnified using a beam expander (Thorlabs BE02-05-B) to cover the aperture of the objective *But why? to focus down to diffraction limit?* and delivered to the interface of the glass plates through a couple of mirrors. HWP and PBS are used to adjust the laser power. A CCD camera (Thorlabs DCC1545M - USB 2.0 CMOS Camera) is placed behind the dichroic mirror to adjust the focusing point by observing the top surface of the upper glass. Z axis of the objective is translated to a position at which laser beam is focused beneath the surface of the bottom glass. The amount to be translated is calculated based on the refractive index and the thickness of the glass sample. Once the focusing point is set, weld seams are generated in the glass to glass interface using a 2D motorized translation stage (Standa 8MTF-102LS05). Translation stage movement is controlled using a stepper & DC motor controller (Standa 8SMC5-USB).

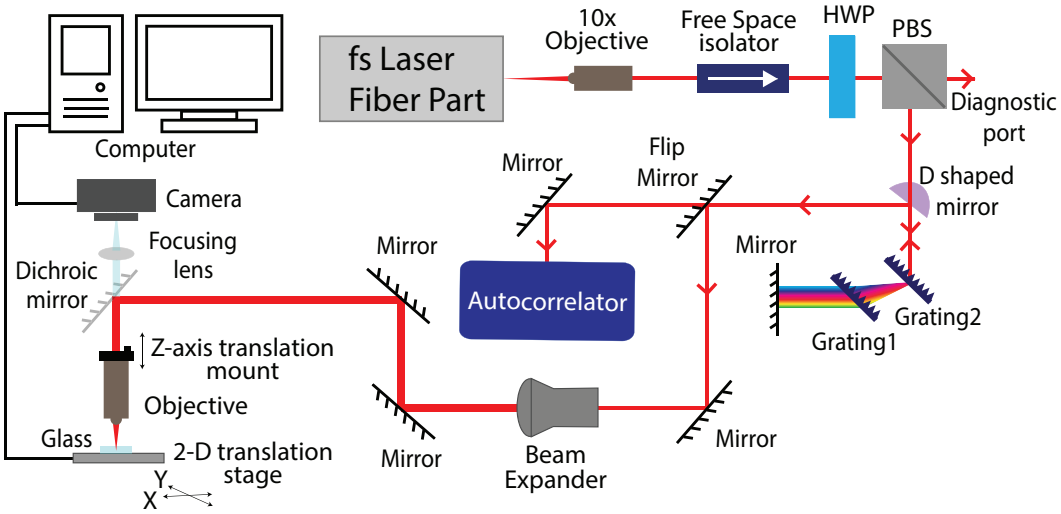

Figure 3.1. Experimental setup for fs laser-glass welding.

3.4. Characterization

The study of modifications in borosilicate glass plates with thickness of 1.1 mm and aluminosilicate glass plates with thickness of 560 μm was conducted using 10x and 20x objectives. Weld lines are generated at different pulse energies and scanning

speeds 200 μm inside glass samples with a separation of 150 μm. The cross-section view of the modifications was obtained by cleaving the glass plates perpendicular to the weld lines utilizing the same laser we built for welding, cleaning the cross-section with acetone and methanol, and imaging by using an optical microscope.

To generate weld seams, optically contacted glass samples are placed on the sample holder which is secured on the translation stage and focused laser beam is scanned along the interface across the optical contact line. To achieve a successful welding, length of the laser-induced welding seams should cover both upper and bottom glass. For this reason, positioning of the laser focus with respect to the interface should be adjusted taking into account the size of the modifications. Figure 3.2 shows (a) the schematic of the inscription process and (b) side view of the laser induced modification in aluminosilicate glass for a pulse energy of 2.75 μJ and translation velocity of 2 mm/s.

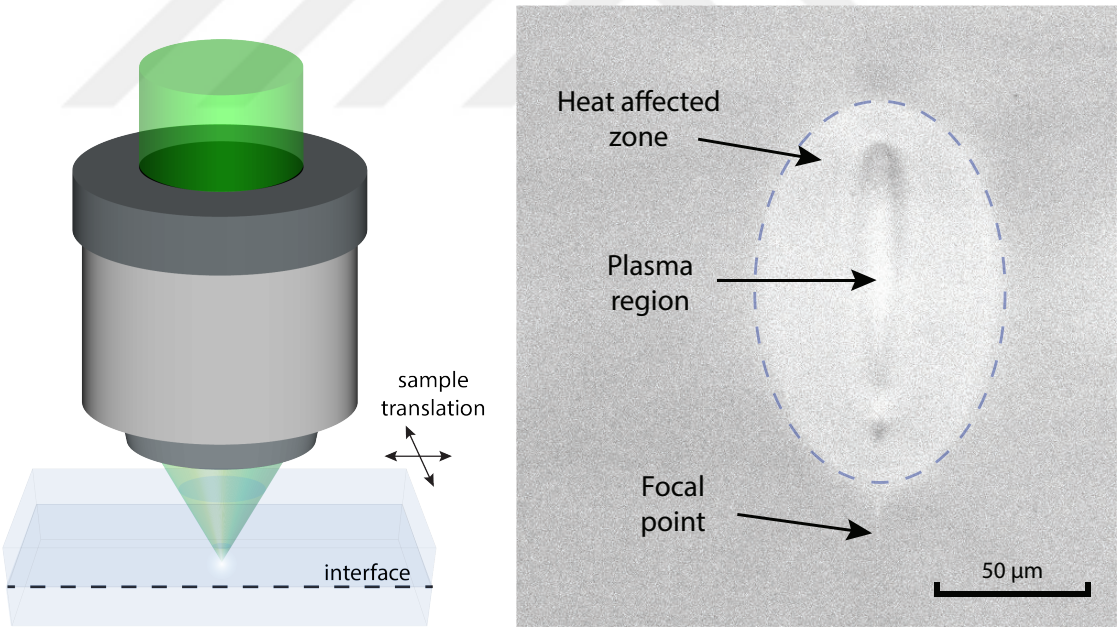

(a) (b)

Figure 3.2. Schematic of the (a) fs laser inscription inside glass and (b) side view of the laser induced modification inside aluminosilicate glass.

3.4.1. Characterization of Heat-Affected Zones in Borosilicate Glasses

To evaluate the size of the modifications, first, we carried out the parameters affecting the heat-affected zone for borosilicate glass plates by changing the scanning

speed of translation stage and pulse energy of the laser. We set the pulse duration at 250 fs and the repetition rate at 400 kHz. Laser pulses were focused to a $\sim$ 3.9 μm diameter in a depth of $\sim$ 100 μm using a 10x objective. We created 3 cm long lines with 150 μm separations by varying the pulse energy and scanning speed. Translation speed is varied between 0.5 - 3.5 mm/s with 0.5 mm/s steps. For each translation speed pulse energy is changed up to 3.5 μJ with 0.2 μJ steps. Figure 3.3 shows the lines obtained by changing the pulse energy for different set of translation speeds. From top to bottom, the scanning speed for each set and the pulse energy used for the inscription of lines within these sets increase.

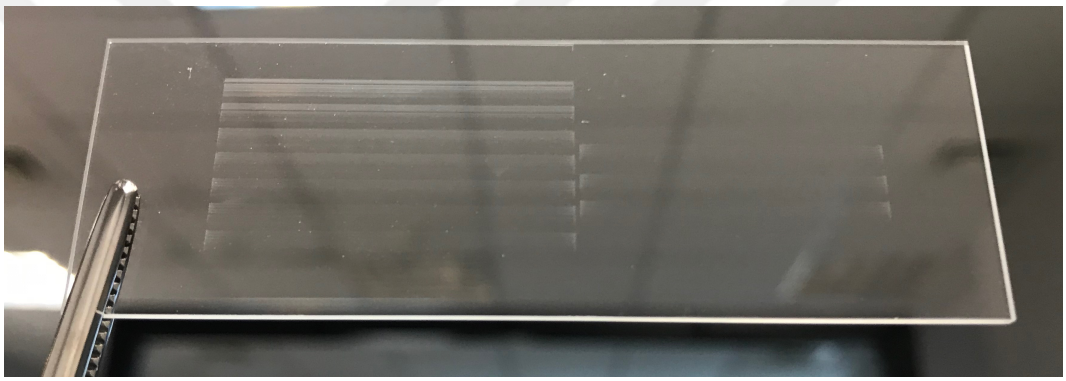

Figure 3.3. Visible lines obtained by changing the pulse energy and scanning speed.

When scanning was completed with these parameters, the glass was cleaved from the middle of the lines and the dimensions of the modifications on the cross section were measured under the microscope. To avoid the acceleration effect of the translation stage when approaching the starting and ending points of the movement, the lines were kept as long as possible and the modifications were examined by cleaving near the midpoints of the lines where the speed of the translation stage is constant. Figure 3.4 and Figure 3.5 show the length and width of the heat-affected zones for the pulse duration at 250 fs and repetition rate at 400 kHz.

Figures show an increase both in length and width as the pulse energy increases for each translation speed. In this case, spot diameter is 3.9 μm, repetition rate is 400 kHz, pulses are separated by 2,5 μs. When translation speed is 1 mm/s, translation amount of the stage between two pulses is calculated to be 2.5 nm, which corresponds to 99.99% overlap between pulses. The amount of the overlap calculated with the same

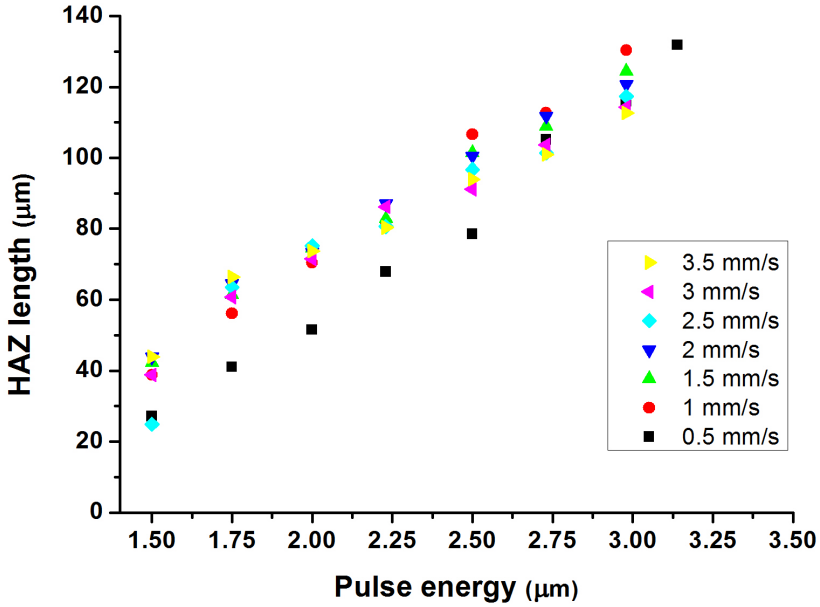

Figure 3.4. Heat affected zone length variation by changing pulse energy and scanning speed at constant repetition rate of 400 kHz.

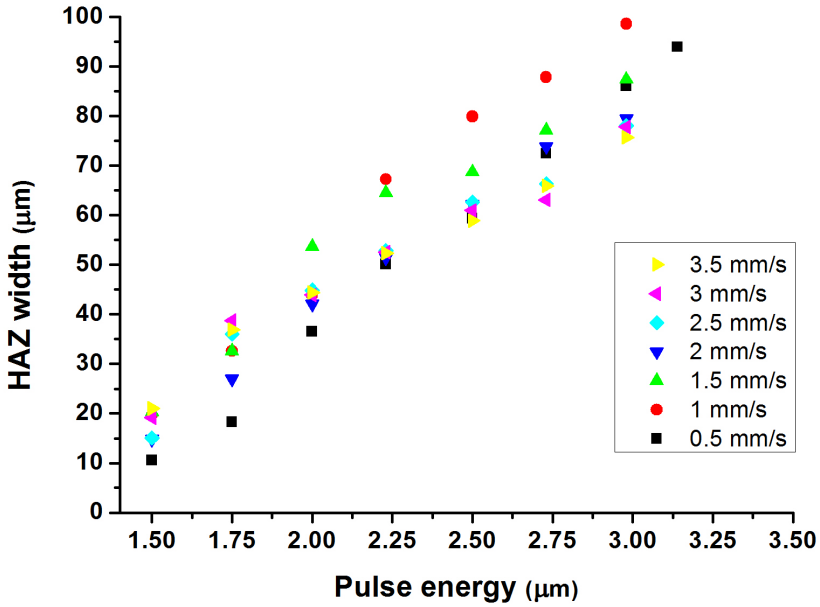

Figure 3.5. Heat affected zone width variation by changing pulse energy and scanning speed at constant repetition rate of 400 kHz.

laser parameters for maximum translation speed 3.5 mm/s in this graph is 99.80%. In this case, the values seen in these graphs are the result of the cumulative effect provided by the high repetition rate rather than the single pulse effect. Due to larger heat

accumulation caused by large spatial overlap, the size of the modifications increases with the increasing pulse energy. The size of the modifications also increases as the translation speed decreases for the same reason, as expected.

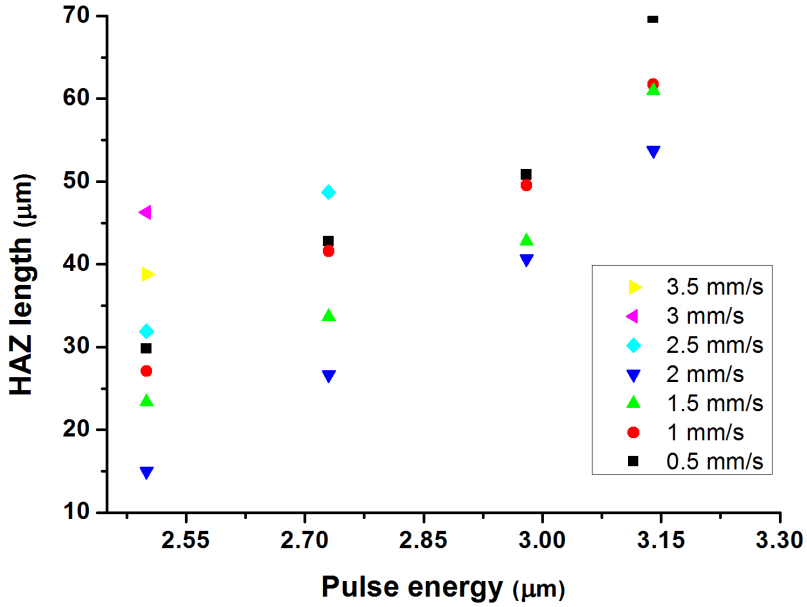

Figure 3.6. Heat affected zone length variation by changing pulse energy and scanning speed at constant repetition rate of 200 kHz.

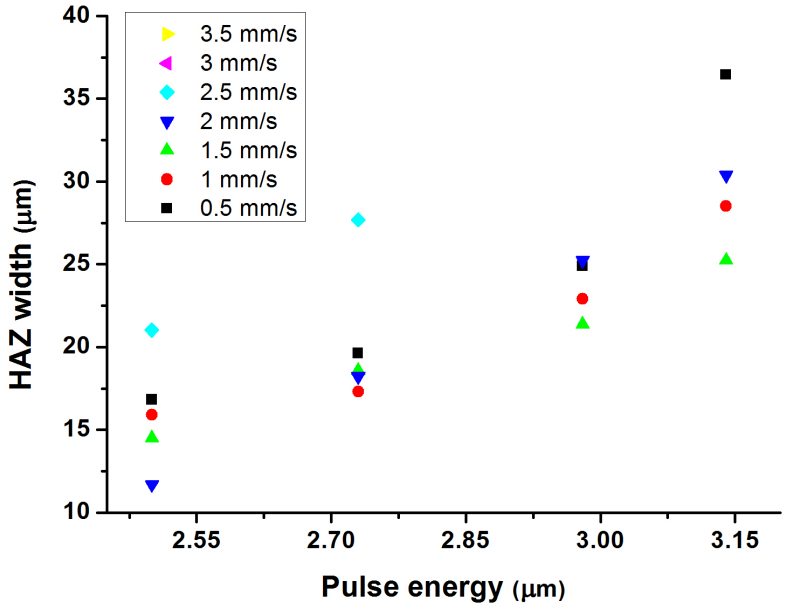

Figure 3.7. Heat affected zone width variation by changing pulse energy and scanning speed at constant repetition rate of 200 kHz.

To investigate the heat accumulation effect on the modified area, we continued with 200 kHz repetition rate. We kept scanning speed and pulse energy the same with the previous case. For each scanning speed, we inscripted lines with the same line spacing. While changing the repetition frequency, we kept the pulse energies at the end of each stage of laser constant and changed the average power accordingly to remain pulse duration unchanged. Figure 3.6 and Figure 3.7 show the change in length and width of heat-affected zones for varying pulse energy and scanning speed at a pulse duration of 250 fs and at a pulse repetition frequency of 200 kHz. Even though we decreased the repetition frequency by half, scanning speeds are still in the order of mm/s. Size of the modifications is increases with the increasing pulse energy and decreasing scanning speed due to heat accumulation. As in the first case, spot diameter is 3.9 μm, but repetition rate is 200 kHz, pulses are separated by 5 μs. When translation speed is 1 mm/s, translation amount of the stage between two pulses is calculated to be 5 nm, which corresponds to 99.99% overlap between pulses. The amount of the overlap calculated with the same laser parameters for maximum translation speed 3.5 mm/s in this graph is 99.56%. Compared to the results seen in Figure 3.3, for the same pulse energy and scanning speeds, lengths of heat-affected zones are about 2-3 times smaller, which proves decreasing repetition rate due to lower hear accumulation results in decreasing modification volume.

We repeated the characterization with a 20x objective (0.4 NA) to observe the fluence effect on the heat affected zones. Spot diameter was calculated to be 2.5 μm. Translation speed is varied between 1 - 10 mm/s with 1 mm/s steps. Pulse energy is increased up to 4 μJ with 0.25 μJ steps at a repetition rate of 400 kHz.

To compare the results with the modifications we have obtained previously using the 10x objective, the trend we expect to see with an increase in the energy and decrease in scanning speed is also present here. This is as expected, due to the increased number of free electrons generated by a higher energy density. Even at 10 mm/s speeds, we had approximately 250 μm heat-affected zone length.

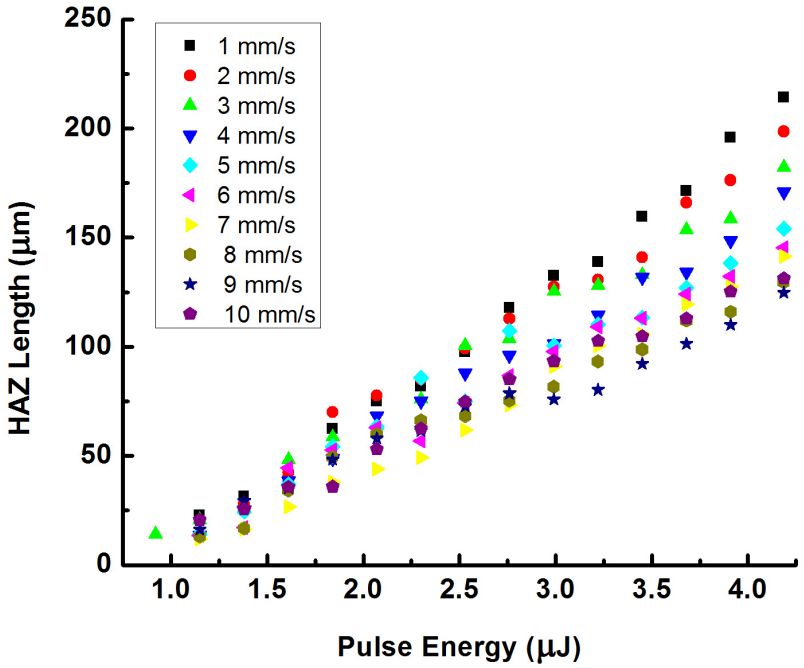

Figure 3.8. Heat affected zone length variation by changing pulse energy and scanning speed at constant repetition rate of 400 kHz, using 0.4 NA objective.

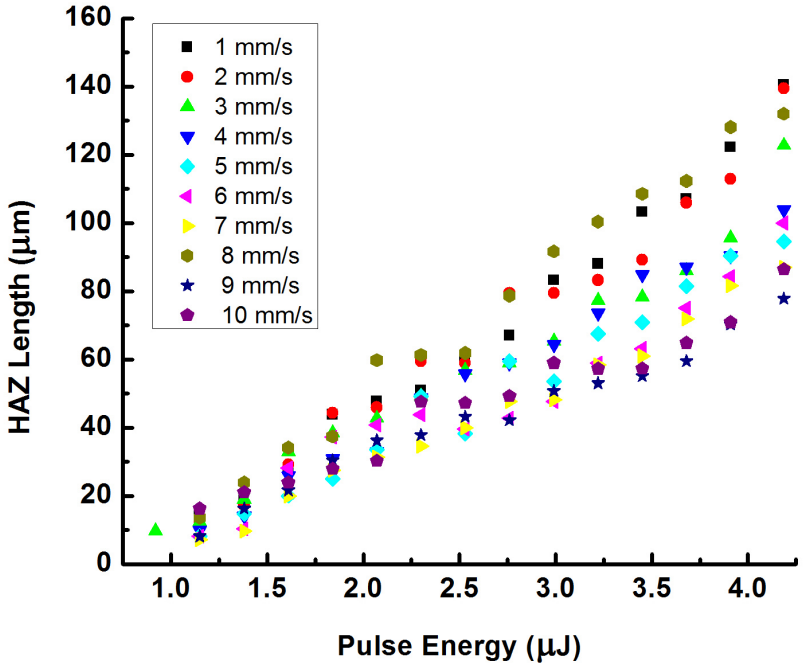

Figure 3.9. Heat affected zone width variation by changing pulse energy and scanning speed at constant repetition rate of 400 kHz, using 0.4 NA objective.

3.4.2. Characterization of Heat-Affected Zones in Aluminosilicate Glasses

For the welding of chemically strengthened aluminosilicate glasses, we made the characterization of heat-affected zones by using the same type of non-strengthened glass.

Glass strengthened by the ion exchange method is well known and used in various glass products, including ophthalmic, optical devices , and cover glass for mobile devices. The process involves producing compressive stress on the surface by replacing smaller ions in the glass, such as sodium or lithium, with larger ions potassium, rubidium or cesium. The resultant stress on the surface is counterbalanced by the tensile tension created in the interior of the glass. This method improves enduring and bending skills of the glass. The compressive stress also enhances the glass surface's ability to withstand mechanical damages. For this reason, compared to normal glasses, it is more difficult to process a strengthened glass that is more resistant to crack formation and fractures with laser. The existence of resistant layers makes traditional mechanical and laser cutting of the ion-exchanged glass difficult or even impossible whereas an increased effort to process these glasses can lead to formation of the chips, resulting in weakened edges.

In order to precisely bond two chemically tempered glass samples we adjusted the size of the laser induced modifications such that the point where compressive strength and tension balance is located below the modifications. Hence, the laser welding seals are adjusted to be smaller than this value by the optimization of the parameters.

In Figure 3.10 and Figure 3.11 length and width of the heat-affected zones formed in aluminosilicate glass using 250 fs pulses at a repetition rate of 400 kHz are shown. According to the chart, laser parameters which gives a HAZ length less than 100 μm were used for the chemically strengthened aluminosilicate glasses. In the first trials, using the same laser parameters, HAZ formation of the same size was not observed in the chemically strengthened glasses. This was most probably due to the chemical treatment that the glass underwent. So we increased to pulse energy and tried with

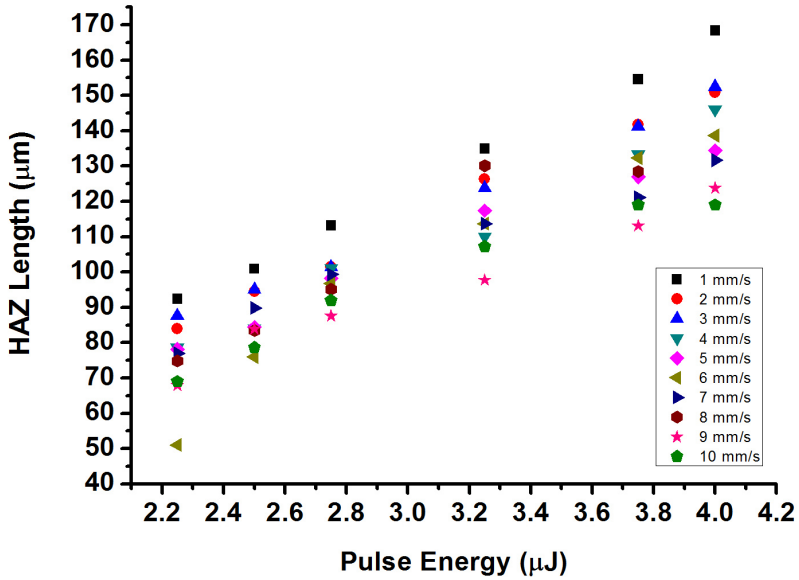

Figure 3.10. HAZ length in aluminosilicate glass using 400 kHz 250 fs pulses.

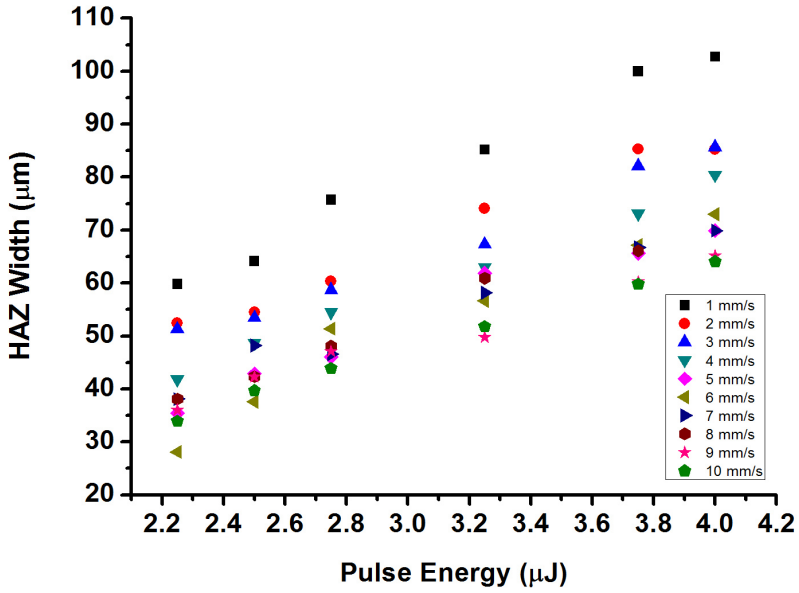

Figure 3.11. HAZ width in aluminosilicate glass using 400 kHz 250 fs pulses.

slower translation speeds. We could achieved successful weldings at a pulse duration of 3.75 μJ. We did not have a method to obtain cross-sectional views without damaging the strengthened glasses, we observed welding seals from the top using an optical microscope. We tested whether the process was successful or not by peeling the two glasses from each other.

3.5. Welding Experiments

3.5.1. Samples

Laser welding of glasses were performed using 2 types of glass. Glass samples are 75 x 25 mm borosilicate glass plates (Borofloat33, SCHOTT Technical Glass Solutions GmbH, Germany) with thickness of 1.1 mm and 25 x 25 mm chemically strengthened aluminosilicate glass plates with thickness of 550 μm. Main reason we have worked with these glasses is that they have low surface roughness (for Borofloat33, roughness $\leq$1 nm RMS) which allows them to bring into sufficiently close contact. Bringing two materials into adequately close contact ensures both of them stays within the focal length of the laser. Too huge gap between the two materials causes ablation of the bottom glass or plasma to escape if the incident energy is not sufficient for development of melt zone to fill the gap.

3.5.2. Cleaning Procedure

All procedures for cleaning glass samples were handled without using an ultrasonic cleaner. Each glass plate was cleaned in two stages using lens tissues (Thorlabs MC-5E Lens Tissues) soaked in acetone and methanol. Acetone is used because it evaporates quickly and it is a good solvent to wipe away any oil from the glass surface. Next, methanol is used to remove the residue acetone leaves. Then, no rinsing were done after methanol and samples were dried by just blowing fresh air. This procedure provided effective removal of the oil and dust particles before making them optically contacted.

After cleaning, the two glasses were placed on top of each other and pressed by hand against each other to create an optical contact. If the two glasses are clean and flat enough, optical contact is achieved and Newton's rings appear immediately without the need of pressing them hard against each other. When it is not perfectly achieved, partially contacted samples should be separated and cleaning procedure must be repeated from the beginning. Once the samples forced into optical contact, Wan der

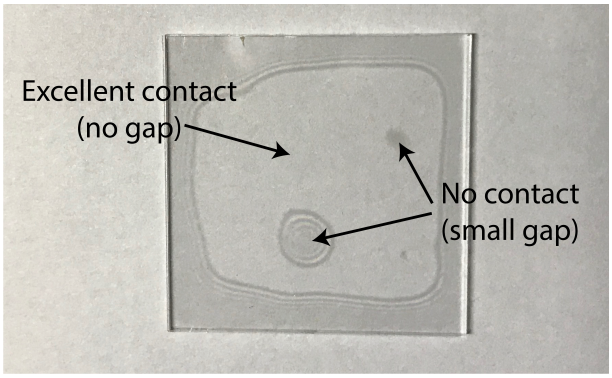

Figure 3.12. Optical contact and no contact regions in two glasses.

Waals forces hold the two samples together. If there is nothing left to cause roughness on the surface in the vicinity of Newton's rings, they remain attached to each other after releasing glasses.

3.5.3. Laser Welding Procedure

Optically contacted glasses were placed on a microscope slide holder which was fixed on the translation stage. We didn't use any extra clamping equipment as the glasses were already optically contacted. Laser beam was focused 15-100 μm inside the bottom glass sample according to the laser parameter used. In the light of the characterization results we made for the glass, we determined how deep the laser focus should be from the interface such that the length of the laser induced modifications cover both the upper and the bottom glass. Looking through the camera which is placed behind the dichroic mirror, we adjusted the spot of the focused laser beam on the top of the upper glass. The displacement length of the z-axis mount between where the focus is on top of the upper glass and just below the interface was calculated using the numerical aperture of the objective and the refractive index of the glass. Then, by translating the z-axis mount downwards, we shifted the focused beam just below the intersection of two glasses.

Following focus adjustment, welding was performed starting from the optically contacted areas. Welds were generated along the glass-glass interface by moving the translation stage utilizing either raster scanning or spiral scanning. Stage movement

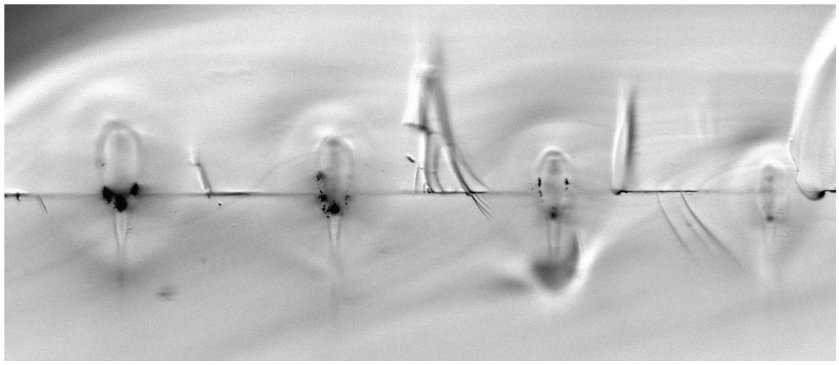

Figure 3.13. Side view of the welded borosilicate glasses after breaking through weld lines.

is controlled and modified by developing a custom motion control software to enable movement in line, rectangle or raster shapes. To minimize the effects of the acceleration of the translation stage on laser-induced modifications while turning the corner points, we defined variable tolerance values for the movement when approaching these points. As a result of this adjustment, crack formation and laser micro-explosions seen at the corner points due to fluence fluctuations decreased to a certain extent.

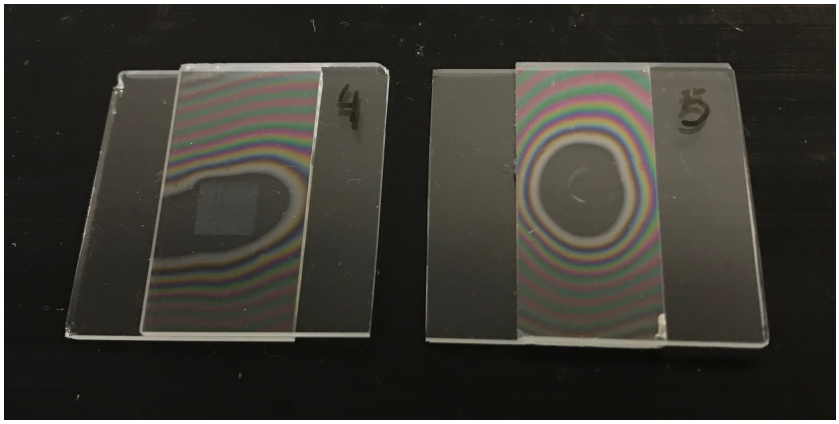

Figure 3.14. Welded borosilicate glasses via raster and spiral shape scanning.

Figure 3.14 shows two borosilicate glass pairs with thickness of 1.1 mm welded with different textures. The one on the left was created with raster scanning, and the one on the right was created with spiral scanning. Both samples were prepared in accordance with the cleaning procedure and optically contacted before welding. For spiral scanning, a rotational step motor placed on the 2-axis translation stage. After the sample is placed on the stepper motor, the point where the beam will fall was adjusted by moving the 2-D stage so that it approximately overlaps with the position of the

rotation axis. While the step motor rotates at a frequency of 2.5 Hz, the translation stage was moved in one direction at a constant speed. Consequently, we obtained spiral weld lines. 3.15 shows two chemically strengthened aluminosilicate glass plates welded with spiral pattern as well.

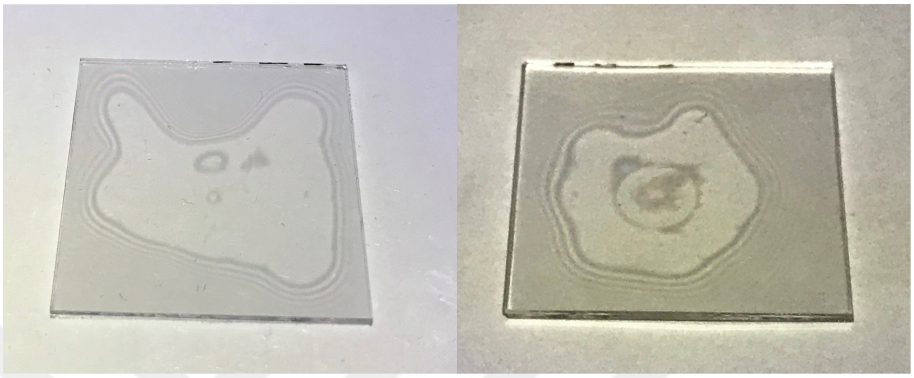

Figure 3.15. Welding of chemically strengthened aluminosilicate glasses using both raster and spiral scanning.

3.6. Weld Strength Measurement

After processing, the samples were optically analyzed by observing the cleaved cross section as mentioned in the characterization part. For the successfully welded samples, the welding strength was measured using a compression testing machine. The reason for choosing the compression test instead of the tensile test is that the tensile test requires an appropriate mechanism to hold the glasses at opposite sides and the glass is more likely to break at those points where it is held while pulling. Figure 3.16 shows the test machine and Figure 3.17 shows a photograph of the welded glasses placed between the plates of the test machine.

The samples to be tested are welded with an overlap and placed between the two plates so that pressure was applied from sides where there are offsets. The size of the sample between the plates and the amount of load to be applied were entered into the software of the machine. Then measurements were executed by compressing the sample in the direction of the applied force until the failure occurred. Applied force were recorded as a function of the displacement.

Figure 3.16. Compression test machine used to test the strength of welding.

Figure 3.18 shows the applied force recorded as a function of deformation which is calculated using displacement while the sample reduces from its initial size. Glass samples used in this strength test weren't correctly aligned and they weren't welded perfectly parallel. Due to this misalignment, uneven stress distribution caused early failures in high stress regions and reduced the load bearing capacity of the sample. The breaks seen in the graph are caused by the cracks that occurred due to high stress at the points where the plates touched to the glasses while they were pressed against each other. At the point where the deformation is 40 %, the drop in the load coincides with the moment when a non-welded corner of the glass is broken because of the misalignment of the glass pieces. When the load capacity reached 160 N, the glass sample was broken outside of the weld area, so the highest compressive force which welded glass samples could withstand could not be measured exactly.

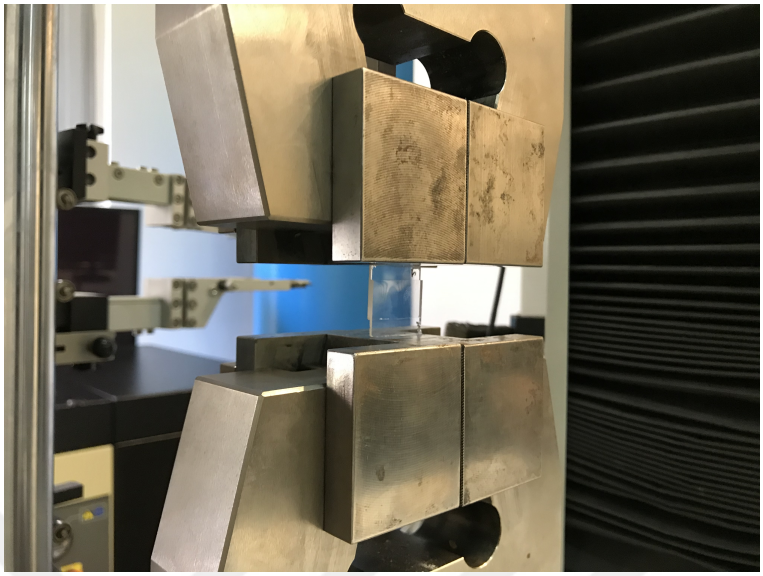

Figure 3.17. Photograph of the welded glass samples inside the compression machine.

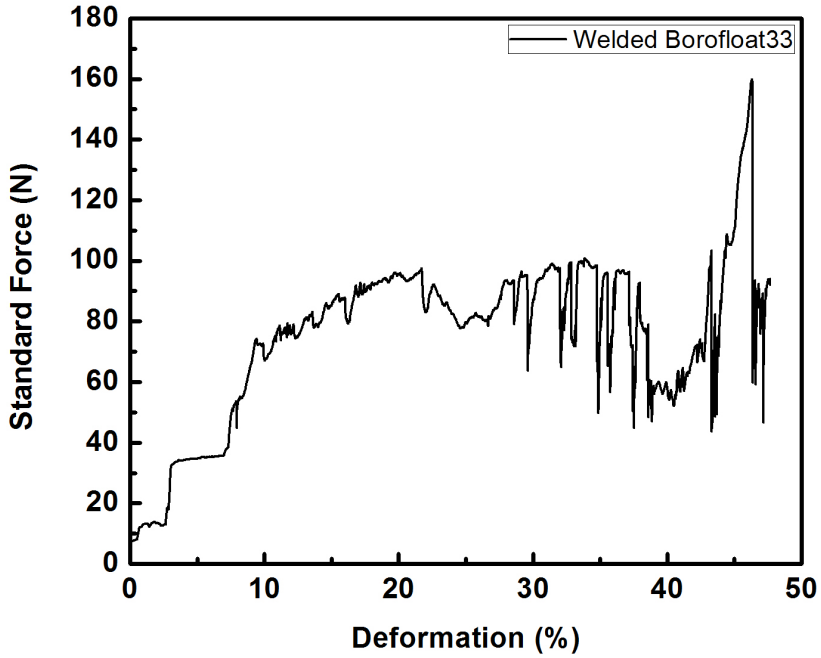

Figure 3.18. Graph showing the applied force onto the sample and the related deformation.

The measured sample was welded using a 10x objective with a pulse energy of 4 μJ and scanning speed of 1 mm/s. The welded area was created by raster scanning with 20 μm spacing. The reason we chose these laser parameters that generates modifications longer than 100 μm is that such a large modification allows a high tolerance for the

positioning of the laser focus with respect to the interface. In addition, the large width with small spacing enables to cover the entire interface by adjacent welding seams in order to gain the highest breaking strength.

Joint strength of the welded glasses were determined by dividing the load by the welding area. Size of the welded area were 0.5 cm x 0.5 cm. Maximum applied force that could be measured were 160 N. For this values, we may conclude that our welded glass samples had a minimum joint strength of 6.8 MPa.

3.7. Preliminary Results of Microfluidic Device Development

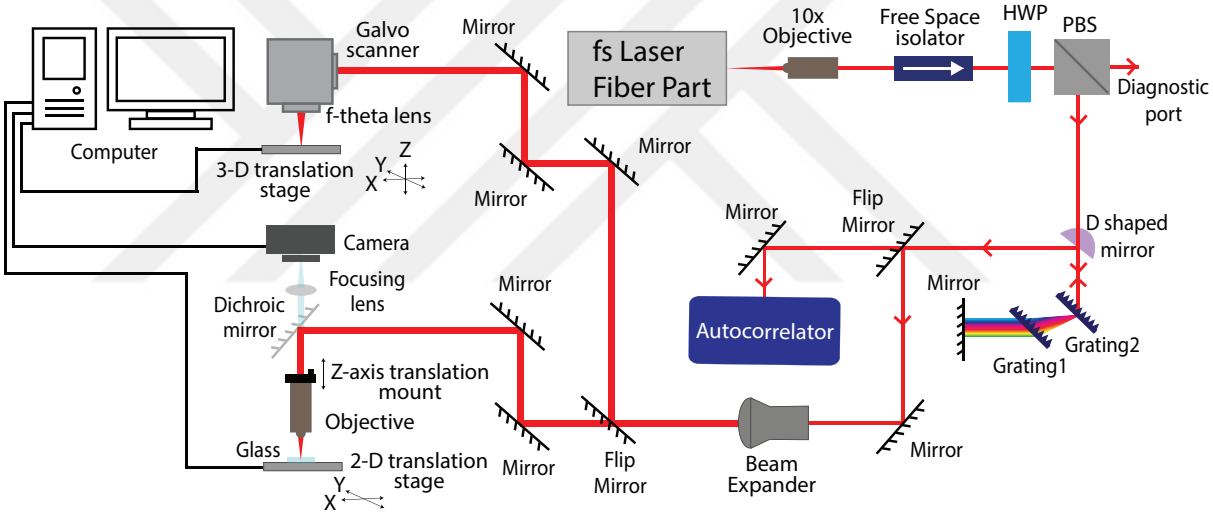

Figure 3.19. Microfluidic channel engraving setup using galvo scanner and fs fiber laser.

Microfluidic patterns were generated using the laser setup shown in Figure 3.19. We have obtained microchannel structures and inlet/outlet ports using Galvo scanner. We used a 56 mm focused f-theta lens to focus the beam onto the sample. The beam radius in the focus was approximately 9 μm. Galvo scanner was controlled using WeldMARK software with a maximum velocity of 4 m/s.

The glass plates were placed on a 3-D translation stage. Geometric patterns entered in the software interface were scanned at the desired speed with the specified scan method and spacing. The inlet and outlet ports were generated by defining circles with a diameter of 1 mm on the glass and scanning the inside of this circle using

cross hatching technique. Two group of parallel lines were chosen to be at 45 degrees. Scanning continued multiple times until the two holes are generated. Channels were processed as straight lines for simplicity. Same procedure repeated for the generation of the channels. In Figure 3.20, optical images of 100 and 300 micrometer thick channels with inlet pools are seen. These patterns were created with 4 μJ pulse energy and 1 mm/s scanning speed.

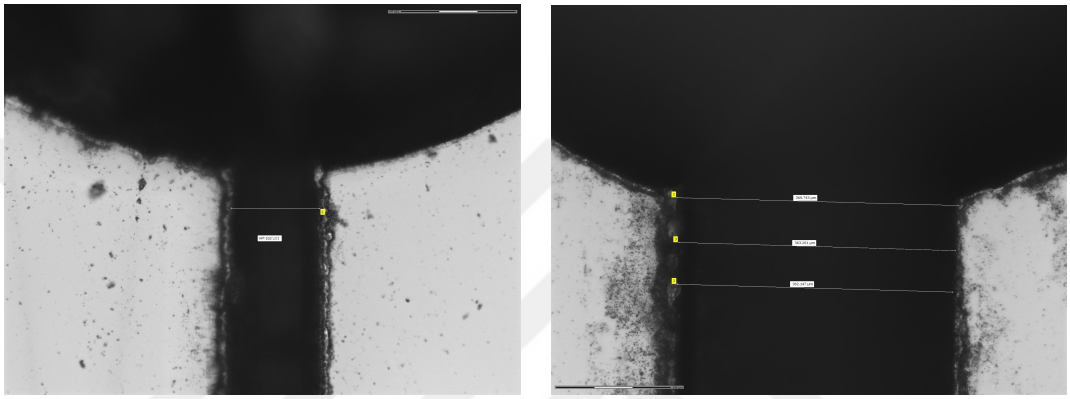

Figure 3.20. Channels that are inscribed onto glass using galvo-scanner and fs laser. (a) 100 micron channel, (b) 300 micron channel.

Following the machining process, each glass plate was cleaned just like in the pre-welding process. The channel structures created were checked by dropping ink into the inlet pool before the second plate was closed. Channels were inspected for any leakage. Inks dropped into the pool passed through the channels without leakage and reached the outlet pool. Bonding of the glass plate with the channel structures and the other plate with inlet/outlet port was performed using laser welding setup described in previous section.

Due to the burrs generated during the micromachining process, two glass plate couldn't be able to bring to an optical contact and we couldn't be able to weld them near the inlet/outlet ports. 3.21 shows the welding process of the partially contacted glass plates. As a result, glass plates were bonded via laser welding but it was only hundred percent successful in the area away from the channels. In order to have two glass plates that are permanently bonded together, we would rub the glasses after the laser treatment.

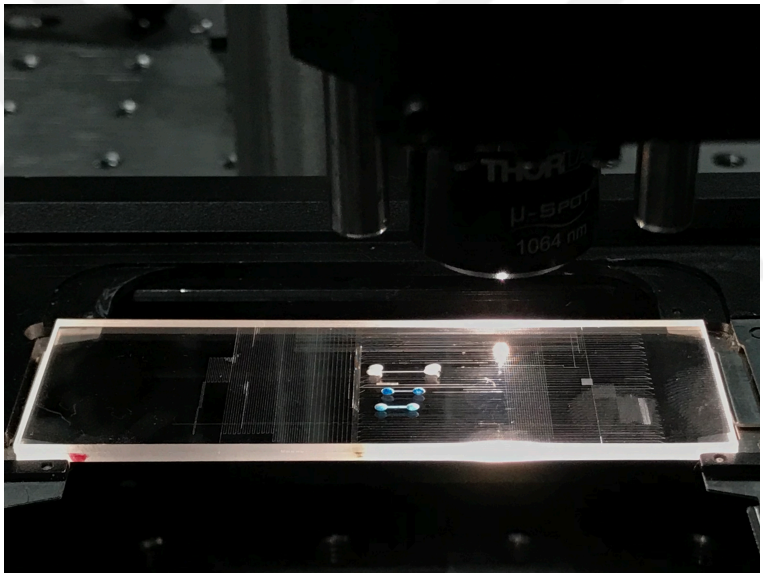

Figure 3.21. A preliminary microfluidic chip made using fs fiber laser.

4. CONCLUSION

In this study, we have built a fs fiber laser system to investigate different parameters for glass welding, which is one of the biggest challenges of glass microfluidic chips. We made the pulse energy, pulse duration and pulse repetition rate adjustable to find the most suitable parameters for different materials and applications. The developed laser is also combined with three different scanning systems to generate adjustable parameters such as pulse repetition rate, pulse duration, pulse energy, fluence, spot size, etc. Affects of some of these parameters are investigated during glass welding. We observed increased molten area for increasing energy and decreasing translation speeds. Successful glass welding is achieved in different materials with different scanning schemes by adjusting the focus point according to the size of the modifications. We achieved adjustable heat affected zone sizes between 10 μm and 250 μm length by changing laser parameters. Thanks to the modification dimensions of these sizes, we have shown that we can weld the glasses without the need for fine focus adjustment. Besides modification dimensions, we investigated how the molten areas formed in the interface are affected by the laser parameters by examining the fluence effect. When we used 20x lens instead of 10x, we saw that voids were formed due to the high energy deposited in the unit area. For this reason, we chose the samples sent to the endurance test from those we did with a 10x lens instead of 20x, although they have the same modification sizes. With the result of the strength test of the glass we have combined, we have shown that femtosecond laser welding is an advantageous method in terms of being fast, requiring less equipment and reproducibility.

Next, a preliminary microfluidic chip is manufactured. Microchannels and inlet/outlet ports were successfully tested. Inks dropped into the canal pools could reach the outlet pool without leaking along the canal. We only had problems welding these two plates since we couldn't get rid of the accumulated material between micromachining and welding processes. This problem could be avoided by polishing the glasses after laser processing with the use of necessary materials.

An infrastructure to manufacture microfluidic chips for biomedical purposes is formed with this thesis work. We saw possible problems and their solutions. In the near future, glass microfluidic chips will be used for Raman spectroscopy and microscopy using this infrastructure. The other adjustable parameters of the laser such as pulse duration, the time between each pulse and polarization of the light will also be investigated to enhance the quality of the chips and obtain better welding. Dissimilar welding, especially ceramics, silicon, glass and metal welding schemes will also be investigated. The combination of different materials will be studied and used in microfluidic chip design with purposes of diagnosis.

REFERENCES

1. Whitesides, G. M., "The Origins and the Future of Microfluidics", *Nature*, Vol. 442, No. 7101, pp. 368–373, 2006.

2. Sackmann, E. K., A. L. Fulton and D. J. Beebe, "The Present and Future Role of Microfluidics in Biomedical Research", *Nature*, Vol. 507, No. 7491, pp. 181–189, 2014.

3. Watanabe, T., F. Sassa, Y. Yoshizumi and H. Suzuki, "Review of Microfluidic Devices for on-Chip Chemical Sensing", *Electronics and Communications in Japan*, Vol. 100, No. 4, pp. 25–32, 2017.

4. Weibel, D. B. and G. M. Whitesides, "Applications of Microfluidics in Chemical Biology", *Current Opinion in Chemical Biology*, Vol. 10, No. 6, pp. 584–591, 2006.

5. Faustino, V., S. O. Catarino, R. Lima and G. Minas, "Biomedical Microfluidic Devices by Using Low-Cost Fabrication Techniques: A Review", *Journal of Biomechanics*, Vol. 49, No. 11, pp. 2280–2292, 2016.

6. Yin, H. and D. Marshall, "Microfluidics for Single Cell Analysis", *Current Opinion in Biotechnology*, Vol. 23, No. 1, pp. 110–119, 2012.

7. Luo, T., L. Fan, R. Zhu and D. Sun, "Microfluidic Single-Cell Manipulation and Analysis: Methods and Applications", *Micromachines*, Vol. 10, No. 2, p. 104, 2019.

8. Nasseri, B., N. Soleimani, N. Rabiee, A. Kalbasi, M. Karimi and M. R. Hamblin, "Point-of-Care Microfluidic Devices for Pathogen Detection", *Biosensors and Bioelectronics*, Vol. 117, pp. 112–128, 2018.

9. Riahi, R., A. Tamayol, S. A. M. Shaegh, A. M. Ghaemmaghami, M. R. Dokmeci and A. Khademhosseini, "Microfluidics for Advanced Drug Delivery Systems", *Current Opinion in Chemical Engineering*, Vol. 7, pp. 101–112, 2015.

10. Sosa-Hernández, J. E., A. M. Villalba-Rodríguez, K. D. Romero-Castillo, M. A. Aguilar-Aguila-Isaías, I. E. García-Reyes, A. Hernández-Antonio, I. Ahmed, A. Sharma, R. Parra-Saldívar and H. Iqbal, "Organs-on-a-Chip Module: A Review from the Development and Applications Perspective", *Micromachines*, Vol. 9, No. 10, p. 536, 2018.

11. McDonald, J. C. and G. M. Whitesides, "Poly (Dimethylsiloxane) as a Material for Fabricating Microfluidic Devices", *Accounts of Chemical Research*, Vol. 35, No. 7, pp. 491–499, 2002.

12. Liga, A., J. A. Morton and M. Kersaudy-Kerhoas, "Safe and Cost-Effective Rapid-Prototyping of Multilayer PMMA Microfluidic Devices", *Microfluidics and Nanofluidics*, Vol. 20, No. 12, p. 164, 2016.

13. Strong, E. B., S. A. Schultz, A. W. Martinez and N. W. Martinez, "Fabrication of Miniaturized Paper-Based Microfluidic Devices (MicroPADs)", *Scientific Reports*, Vol. 9, No. 1, pp. 1–9, 2019.

14. Koo, H.-J. and O. D. Velev, "Design and Characterization of Hydrogel-Based Microfluidic Devices with Biomimetic Solute Transport Networks", *Biomicrofluidics*, Vol. 11, No. 2, p. 024104, 2017.

15. Leester-Schädel, M., T. Lorenz, F. Jürgens and C. Richter, "Fabrication of Microfluidic Devices", *Microsystems for Pharmatechnology*, pp. 23–57, Springer, 2016.

16. Iliescu, C., H. Taylor, M. Avram, J. Miao and S. Franssila, "A Practical Guide for the Fabrication of Microfluidic Devices Using Glass and Silicon", *Biomicrofluidics*, Vol. 6, No. 1, p. 016505, 2012.

17. Gale, B. K., A. R. Jafek, C. J. Lambert, B. L. Goenner, H. Moghimifam, U. C. Nze and S. K. Kamarapu, "A Review of Current Methods in Microfluidic Device Fabrication and Future Commercialization Prospects", *Inventions*, Vol. 3, No. 3, p. 60, 2018.

18. Yang, Y., E. Noviana, M. P. Nguyen, B. J. Geiss, D. S. Dandy and C. S. Henry, "Paper-Based Microfluidic Devices: Emerging Themes and Applications", *Analytical Chemistry*, Vol. 89, No. 1, pp. 71–91, 2017.

19. Ho, C. M. B., S. H. Ng, K. H. H. Li and Y.-J. Yoon, "3D Printed Microfluidics for Biological Applications", *Lab on a Chip*, Vol. 15, No. 18, pp. 3627–3637, 2015.

20. Mahmoodi, M., S. Mahdavi, L. A. James and T. Johansen, "A Quick Method to Fabricate Large Glass Micromodel Networks", *Microsystem Technologies*, Vol. 24, No. 5, pp. 2419–2427, 2018.

21. Chen, J., R. M. Carter, R. R. Thomson and D. P. Hand, "Avoiding the Requirement for Pre-Existing Optical Contact During Picosecond Laser Glass-to-Glass Welding", *Optics Express*, Vol. 23, No. 14, pp. 18645–18657, 2015.

22. Fu, L.-M., W.-J. Ju, R.-J. Yang and Y.-N. Wang, "Rapid Prototyping of Glass-Based Microfluidic Chips Utilizing Two-Pass Defocused CO_2 Laser Beam Method", *Microfluidics and Nanofluidics*, Vol. 14, No. 3-4, pp. 479–487, 2013.

23. Queste, S., R. Salut, S. Clatot, J.-Y. Rauch and C. G. K. Malek, "Manufacture of Microfluidic Glass Chips by Deep Plasma Etching, Femtosecond Laser Ablation, and Anodic Bonding", *Microsystem Technologies*, Vol. 16, No. 8-9, pp. 1485–1493, 2010.

24. Matsuo, S., H. Sumi, S. Kiyama, T. Tomita and S. Hashimoto, "Femtosecond Laser-Assisted Etching of Pyrex Glass with Aqueous Solution of KOH", *Applied Surface Science*, Vol. 255, No. 24, pp. 9758–9760, 2009.

25. Zimmermann, F., S. Richter, S. Döring, A. Tünnermann and S. Nolte, "Ultrastable Bonding of Glass with Femtosecond Laser Bursts", *Applied Optics*, Vol. 52, No. 6, pp. 1149–1154, 2013.

26. Gattass, R. R. and E. Mazur, "Femtosecond Laser Micromachining in Transparent Materials", *Nature Photonics*, Vol. 2, No. 4, pp. 219–225, 2008.

27. Sugioka, K. and Y. Cheng, "Ultrafast Lasers—Reliable Tools for Advanced Materials Processing", *Light: Science & Applications*, Vol. 3, No. 4, pp. e149–e149, 2014.

28. Tamaki, T., W. Watanabe, J. Nishii and K. Itoh, "Welding of Transparent Materials Using Femtosecond Laser Pulses", *Japanese Journal of Applied Physics*, Vol. 44, No. 5L, p. L687, 2005.

29. Okamoto, Y., I. Miyamoto, K. Cvecek, A. Okada, K. Takahashi and M. Schmidt, "Evaluation of Molten Zone in Micro-Welding of Glass by Picosecond Pulsed Laser", *Journal of Laser Micro/Nanoengineering*, Vol. 8, No. 1, 2013.

30. Huang, H., L.-M. Yang and J. Liu, "Direct Welding of Fused Silica with Femtosecond Fiber Laser", *Laser-Based Micro-and Nanopackaging and Assembly Vi*, Vol. 8244, p. 824403, International Society for Optics and Photonics, 2012.

31. Cvecek, K., R. Odato, S. Dehmel, I. Miyamoto and M. Schmidt, "Gap Bridging in Joining of Glass Using Ultra Short Laser Pulses", *Optics Express*, Vol. 23, No. 5, pp. 5681–5693, 2015.

32. Blow, K. J. and D. Wood, "Theoretical Description of Transient Stimulated Raman Scattering in Optical Fibers", *IEEE Journal of Quantum Electronics*, Vol. 25, No. 12, pp. 2665–2673, 1989.

33. Xu, C. and F. Wise, "Recent Advances in Fibre Lasers for Nonlinear Microscopy", *Nature Photonics*, Vol. 7, No. 11, pp. 875–882, 2013.

34. Liu, X., D. Du and G. Mourou, "Laser Ablation and Micromachining with Ultrashort Laser Pulses", *IEEE Journal of Quantum Electronics*, Vol. 33, No. 10, pp. 1706–1716, 1997.

35. Lubatschowski, H., "Ultrafast Lasers in Ophthalmology", *Physics Procedia*, Vol. 5, pp. 637–640, 2010.

36. Ohta, H., S. Nogiwa, N. Oda and H. Chiba, "Highly Sensitive Optical Sampling System Using Timing-Jitter-Reduced Gain-Switched Optical Pulse", *Electronics Letters*, Vol. 33, No. 25, pp. 2142–2144, 1997.

37. Udem, T., R. Holzwarth and T. W. Hänsch, "Optical Frequency Metrology", *Nature*, Vol. 416, No. 6877, pp. 233–237, 2002.

38. Poole, S., D. N. Payne and M. Fermann, "Fabrication of Low-Loss Optical Fibres Containing Rare-Earth Ions", *Electronics Letters*, Vol. 21, No. 17, pp. 737–738, 1985.

39. Mears, R., L. Reekie, S. Poole and D. Payne, "Neodymium-Doped Silica Single-Mode Fibre Lasers", *Electronics Letters*, Vol. 21, No. 17, pp. 738–740, 1985.

40. Mears, R. J., L. Reekie, I. Jauncey and D. N. Payne, "Low-Noise Erbium-Doped Fibre Amplifier Operating at 1.54 μm", *Electronics Letters*, Vol. 23, No. 19, pp. 1026–1028, 1987.

41. Po, H., E. Snitzer, R. Tumminelli, L. Zenteno, F. Hakimi, N. M. Cho and T. Haw, "Double Clad High Brightness Nd Fiber Laser Pumped by GaAlAs Phased Array", *Optical Fiber Communication Conference*, p. PD7, Optical Society of America, 1989.

42. Liem, A., T. Limpert, H. Zellmer, A. Tunnermann, V. Reichel, K. Morl, S. Jetschke, S. Unger, H.-P. Muller, J. Kirchhof *et al.*, "1.3 kW Yb-Doped Fiber Laser with Excellent Beam Quality", *Conference on Lasers and Electro-Optics,*

2004.(CLEO)., Vol. 2, pp. 1067–1068, IEEE, 2004.

43. Hanna, D., R. Percival, I. Perry, R. Smart, P. Suni, J. Townsend and A. Tropper, "Continuous-Wave Oscillation of a Monomode Ytterbium-Doped Fibre Laser", *Electronics Letters*, Vol. 24, No. 17, pp. 1111–1113, 1988.

44. Lee, Y., S. Sinha, M. Digonnet, R. Byer and S. Jiang, "Measurement of High Photodarkening Resistance in Heavily Yb3+-Doped Phosphate Fibres", *Electronics Letters*, Vol. 44, No. 1, pp. 14–16, 2008.

45. Morasse, B., S. Chatigny, É. Gagnon, C. Hovington, J.-P. Martin and J.-P. de Sandro, "Low Photodarkening Single Cladding Ytterbium Fiber Amplifier", *Fiber Lasers IV: Technology, Systems, and Applications*, Vol. 6453, p. 64530H, International Society for Optics and Photonics, 2007.

46. Lamb Jr, W. E., "Theory of an Optical Maser", *Physical Review*, Vol. 134, No. 6A, p. A1429, 1964.

47. Mollenauer, L. F. and R. H. Stolen, "The Soliton Laser", *Optics News*, Vol. 10, No. 6, pp. 20_2–21, 1984.

48. Blow, K. and B. Nelson, "Improved Mode Locking of an F-Center Laser with a Nonlinear Nonsoliton External Cavity", *Optics Letters*, Vol. 13, No. 11, pp. 1026–1028, 1988.

49. Spence, D. E., P. N. Kean and W. Sibbett, "60-fsec Pulse Generation From a Self-Mode-Locked Ti: Sapphire Laser", *Optics Letters*, Vol. 16, No. 1, pp. 42–44, 1991.

50. Keller, U., D. Miller, G. Boyd, T. Chiu, J. Ferguson and M. Asom, "Solid-State Low-Loss Intracavity Saturable Absorber for Nd: YLF Lasers: An Antiresonant Semiconductor Fabry–Perot Saturable Absorber", *Optics Letters*, Vol. 17, No. 7, pp. 505–507, 1992.

51. Fermann, M., M. Hofer, F. Haberl and S. Craig-Ryan, "Femtosecond Fibre Laser", *Electronics Letters*, Vol. 26, No. 20, pp. 1737–1738, 1990.

52. Fermann, M. E., M. Hofer, F. Haberl, A. Schmidt and L. Turi, "Additive-Pulse-Compression Mode Locking of a Neodymium Fiber Laser", *Optics Letters*, Vol. 16, No. 4, pp. 244–246, 1991.

53. Hofer, M., M. Ober, F. Haberl and M. Fermann, "Characterization of Ultrashort Pulse Formation in Passively Mode-Locked Fiber Lasers", *IEEE Journal of Quantum Electronics*, Vol. 28, No. 3, pp. 720–728, 1992.

54. Duling, I. N., "All-Fiber Ring Soliton Laser Mode Locked with a Nonlinear Mirror", *Optics Letters*, Vol. 16, No. 8, pp. 539–541, 1991.

55. Cautaerts, V., D. Richardson, R. Paschotta and D. Hanna, "Stretched Pulse Yb 3+: Silica Fiber Laser", *Optics Letters*, Vol. 22, No. 5, pp. 316–318, 1997.

56. Nelson, L., K. Tamura, E. Ippen and H. Haus, "Additive-Pulse Mode-Locked Thulium-Doped Fiber Ring Laser", *Conference on Lasers and Electro-Optics*, p. CWI4, Optical Society of America, 1995.

57. Zhou, X., D. Yoshitomi, Y. Kobayashi, S. Tani, H. Yokoi and K. Torizuka, "Generation of Sub-30 fs Pulses From a Mode-Locked Ytterbium Fiber Laser Oscillator with Phase Compensation", *Conference on Lasers and Electro-Optics*, p. CFP7, Optical Society of America, 2008.

58. Ma, C., A. Khanolkar, Y. Zang and A. Chong, "Ultrabroadband, Few-Cycle Pulses Directly From a Mamyshev Fiber Oscillator", *Photonics Research*, Vol. 8, No. 1, pp. 65–69, 2020.

59. Fermann, M., M. Andrejco, Y. Silberberg and M. Stock, "Passive Mode Locking by Using Nonlinear Polarization Evolution in a Polarization-Maintaining Erbium-Doped Fiber", *Optics Letters*, Vol. 18, No. 11, pp. 894–896, 1993.

60. Haus, H. A., J. G. Fujimoto and E. P. Ippen, "Analytic Theory of Additive Pulse and Kerr Lens Mode Locking", *IEEE Journal of Quantum Electronics*, Vol. 28, No. 10, pp. 2086–2096, 1992.

61. Chen, Y., F. Kärtner, U. Morgner, S. Cho, H. Haus, E. Ippen and J. Fujimoto, "Dispersion-Managed Mode Locking", *Journal of the Optical Society of America B*, Vol. 16, No. 11, 1999.

62. Kafka, J., T. Baer and D. W. Hall, "Mode-Locked Erbium-Doped Fiber Laser with Soliton Pulse Shaping", *Optics Letters*, Vol. 14, No. 22, pp. 1269–1271, 1989.

63. Ilday, F., J. Buckley, W. Clark and F. Wise, "Self-Similar Evolution of Parabolic Pulses in a Laser", *Physical Review Letters*, Vol. 92, No. 21, p. 213902, 2004.

64. Fermann, M., K. Sugden and I. Bennion, "High-Power Soliton Fiber Laser Based on Pulse Width Control with Chirped Fiber Bragg Gratings", *Optics Letters*, Vol. 20, No. 2, pp. 172–174, 1995.

65. Fermann, M., K. Sugden and I. Bennion, "Generation of 10 nJ Picosecond Pulses From a Modelocked Fibre Laser", *Electronics Letters*, Vol. 31, No. 3, pp. 194–195, 1995.

66. Tamura, K., E. Ippen, H. Haus and L. Nelson, "77-fs Pulse Generation From a Stretched-Pulse Mode-Locked All-Fiber Ring Laser", *Optics Letters*, Vol. 18, No. 13, pp. 1080–1082, 1993.

67. Brabec, T., C. Spielmann and F. Krausz, "Limits of Pulse Shortening in Solitary Lasers", *Optics Letters*, Vol. 17, No. 10, pp. 748–750, 1992.

68. Gouveia-Neto, A., A. Sombra, P. Wigley and J. Taylor, "Amplification of Picosecond Pulses in Neodymium-Doped Single-Mode Optical Fibres", *Journal of Modern Optics*, Vol. 36, No. 9, pp. 1143–1150, 1989.

69. Suzuki, K., Y. Kimura and M. Nakazawa, "Subpicosecond Soliton Amplification and Transmission Using Er 3+-Doped Fibers Pumped by InGaAsP Laser Diodes", *Optics Letters*, Vol. 14, No. 16, pp. 865–867, 1989.

70. Khrushchev, I. Y., A. Grudinin, E. Dianov, D. Korobkin, V. Semenov and A. Prokhorov, "Amplification of Femtosecond Pulses in Er/sup 3+/-Doped Single-Mode Optical Fibres", *Electronics Letters*, Vol. 26, No. 7, pp. 456–458, 1990.

71. Richardson, D., V. V. Afanasjev, A. Grudinin and D. N. Payne, "Amplification of Femtosecond Pulses in a Passive, All-Fiber Soliton Source", *Optics Letters*, Vol. 17, No. 22, pp. 1596–1598, 1992.

72. Shirakawa, A., J. Ota, M. Musha, K. Nakagawa, K.-i. Ueda, J. R. Folkenberg and J. Broeng, "Large-Mode-Area Erbium-Ytterbium-Doped Photonic-Crystal Fiber Amplifier for High-Energy Femtosecond Pulses at 1.55 μm", *Optics Express*, Vol. 13, No. 4, pp. 1221–1227, 2005.

73. Strickland, D. and G. Mourou, "Compression of Amplified Chirped Optical Pulses", *Optics Communications*, Vol. 56, No. 3, pp. 219–221, 1985.

74. Paschotta, R. *et al.*, *Encyclopedia of Laser Physics and Technology*, Vol. 1, Wiley Online Library, 2008.

75. Galvanauskas, A., M. Fermann, D. Harter, K. Sugden and I. Bennion, "All-Fiber Femtosecond Pulse Amplification Circuit Using Chirped Bragg Gratings", *Applied Physics Letters*, Vol. 66, No. 9, pp. 1053–1055, 1995.

76. Galvanauskas, A., A. Heaney, T. Erdogan and D. Harter, "Use of Volume Chirped Bragg Gratings for Compact High-Energy Chirped Pulse Amplification Circuits", *Technical Digest. Summaries of Papers Presented at the Conference on Lasers and Electro-Optics. Conference Edition. 1998 Technical Digest Series, Vol. 6 (IEEE Cat. No. 98CH36178)*, p. 362, IEEE, 1998.

77. Hartl, I., T. Schibli, A. Marcinkevicius, D. Yost, D. Hudson, M. Fermann and J. Ye, "Cavity-Enhanced Similariton Yb-Fiber Laser Frequency Comb: 3×10^{14} W/cm^2 Peak Intensity at 136 MHz", *Optics Letters*, Vol. 32, No. 19, pp. 2870–2872, 2007.

78. Fermann, M., M. Stock, A. Galvanauskas, G. Cho and B. Thomsen, "Third-Order Dispersion Control in Ultrafast Yb Fiber Amplifiers", *Advanced Solid State Lasers*, p. TuA3, Optical Society of America, 2001.

79. Wysocki, P. F., J. R. Simpson and D. Lee, "Prediction of Gain Peak Wavelength for Er-Doped Fiber Amplifiers and Amplifier Chains", *IEEE Photonics Technology Letters*, Vol. 6, No. 9, pp. 1098–1100, 1994.

80. Kane, S., J. Squier, J. Rudd and G. Mourou, "Hybrid Grating–Prism Stretcher–Compressor System with Cubic Phase and Wavelength Tunability and Decreased Alignment Sensitivity", *Optics Letters*, Vol. 19, No. 22, pp. 1876–1878, 1994.

81. Dong, L., "Approximate Treatment of the Nonlinear Waveguide Equation in the Regime of Nonlinear Self-Focus", *Journal of Lightwave Technology*, Vol. 26, No. 20, pp. 3476–3485, 2008.

82. Stuart, B. C., M. D. Feit, S. Herman, A. Rubenchik, B. Shore and M. Perry, "Nanosecond-to-Femtosecond Laser-Induced Breakdown in Dielectrics", *Physical Review B*, Vol. 53, No. 4, p. 1749, 1996.

83. Smith, A., B. Do, R. Schuster and D. Collier, "Rate Equation Model of Bulk Optical Damage of Silica, and the Influence of Polishing on Surface Optical Damage of Silica", *Fiber Lasers V: Technology, Systems, and Applications*, Vol. 6873, p. 68730U, International Society for Optics and Photonics, 2008.

84. Yavaş, S., M. Erdogan, K. Gürel, F. Ö. Ilday, Y. B. Eldeniz and U. H. Tazebay, "Fiber Laser-Microscope System for Femtosecond Photodisruption of Biological Samples", *Biomedical Optics Express*, Vol. 3, No. 3, pp. 605–611, 2012.

85. Tamaki, T., W. Watanabe and K. Itoh, "Laser Micro-Welding of Transparent Materials by a Localized Heat Accumulation Effect Using a Femtosecond Fiber Laser at 1558 nm", *Optics Express*, Vol. 14, No. 22, pp. 10460–10468, 2006.

86. Miyamoto, I., A. Horn, J. Gottmann, D. Wortmann and F. Yoshino, "Fusion Welding of Glass Using Femtosecond Laser Pulses with High-Repetition Rates", *Journal of Laser Micro/Nanoengineering*, Vol. 2, No. 1, pp. 57–63, 2007.

87. Miyamoto, I., K. Cvecek, Y. Okamoto and M. Schmidt, "Novel Fusion Welding Technology of Glass Using Ultrashort Pulse Lasers", *Physics Procedia*, Vol. 5, pp. 483–493, 2010.

88. Richter, S., F. Zimmermann, R. Eberhardt, A. Tünnermann and S. Nolte, "Toward Laser Welding of Glasses Without Optical Contacting", *Applied Physics A*, Vol. 121, No. 1, pp. 1–9, 2015.

89. Cvecek, K., I. Alexeev, I. Miyamoto and M. Schmidt, "Defect Formation in Glass Welding by Means of Ultra Short Laser Pulses", *Physics Procedia*, Vol. 5, pp. 495–502, 2010.

90. Chen, H., L. Deng, J. Duan and X. Zeng, "Picosecond Laser Welding of Glasses with a Large Gap by a Rapid Oscillating Scan", *Optics Letters*, Vol. 44, No. 10, pp. 2570–2573, 2019.

91. Kongsuwan, P., G. Satoh and Y. L. Yao, "Transmission Welding of Glass by Femtosecond Laser: Mechanism and Fracture Strength", *Journal of Manufacturing Science and Engineering*, Vol. 134, No. 1, 2012.

92. Miyamoto, I., K. Cvecek, Y. Okamoto, M. Schmidt and H. Helvajian, "Characteristics of Laser Absorption and Welding in FOTURAN Glass by Ultrashort Laser Pulses", *Optics Express*, Vol. 19, No. 23, pp. 22961–22973, 2011.

93. Watanabe, W., S. Onda, T. Tamaki, K. Itoh and J. Nishii, "Space-Selective Laser Joining of Dissimilar Transparent Materials Using Femtosecond Laser Pulses", *Applied Physics Letters*, Vol. 89, No. 2, p. 021106, 2006.

94. Hélie, D., F. Lacroix and R. Vallée, "Reinforcing a Direct Bond Between Optical Materials by Filamentation Based Femtosecond Laser Welding", *Journal of Laser Micro Nanoengineering*, Vol. 7, No. 3, p. 284, 2012.

95. Carter, R. M., J. Chen, J. D. Shephard, R. R. Thomson and D. P. Hand, "Picosecond Laser Welding of Similar and Dissimilar Materials", *Applied Optics*, Vol. 53, No. 19, pp. 4233–4238, 2014.

96. Utsumi, A., T. Ooie, T. Yano and M. Katsumura, "Direct Bonding of Glass and Metal Using Short Pulsed Laser", *Journal of Laser Micro/Nanoengineering.*, Vol. 2, pp. 133–136, 2007.

97. Zhang, G., J. Bai, W. Zhao, K. Zhou and G. Cheng, "Interface Modification Based Ultrashort Laser Microwelding Between SiC and Fused Silica", *Optics Express*, Vol. 25, No. 3, pp. 1702–1709, 2017.

98. Temiz, Y., R. D. Lovchik, G. V. Kaigala and E. Delamarche, "Lab-on-a-Chip Devices: How to Close and Plug the Lab?", *Microelectronic Engineering*, Vol. 132, pp. 156–175, 2015.

99. Tamrin, K., Y. Nukman and S. Zakariyah, "Laser Lap Joining of Dissimilar Materials: A Review of Factors Affecting Joint Strength", *Materials and Manufacturing Processes*, Vol. 28, No. 8, pp. 857–871, 2013.

100. Weber, M. J., *Handbook of Optical Materials*, Vol. 19, CRC Press, 2002.

101. Topcu, T. and F. Robicheaux, "Dichotomy Between Tunneling and Multiphoton Ionization in Atomic Photoionization: Keldysh Parameter γ versus Scaled Frequency Ω", *Physical Review A*, Vol. 86, No. 5, p. 053407, 2012.

102. Diels, J.-C. and W. Rudolph, *Ultrashort Laser Pulse Phenomena*, Elsevier, 2006.

103. Schaffer, C. B., A. Brodeur and E. Mazur, "Laser-Induced Breakdown and Damage in Bulk Transparent Materials Induced by Tightly Focused Femtosecond Laser Pulses", *Measurement Science and Technology*, Vol. 12, No. 11, p. 1784, 2001.

104. Lenzner, M., J. Krüger, S. Sartania, Z. Cheng, C. Spielmann, G. Mourou, W. Kautek and F. Krausz, "Femtosecond Optical Breakdown in Dielectrics", *Physical Review Letters*, Vol. 80, No. 18, p. 4076, 1998.

105. Miyamoto, I., K. Cvecek and M. Schmidt, "Evaluation of Nonlinear Absorptivity in Internal Modification of Bulk Glass by Ultrashort Laser Pulses", *Optics Express*, Vol. 19, No. 11, pp. 10714–10727, 2011.

106. Itoh, K., W. Watanabe, S. Nolte and C. B. Schaffer, "Ultrafast Processes for Bulk Modification of Transparent Materials", *MRS Bulletin*, Vol. 31, No. 8, pp. 620–625, 2006.

107. Davis, K. M., K. Miura, N. Sugimoto and K. Hirao, "Writing Waveguides in Glass with a Femtosecond Laser", *Optics Letters*, Vol. 21, No. 21, pp. 1729–1731, 1996.

108. Cvecek, K., S. Dehmel, I. Miyamoto and M. Schmidt, "A Review on Glass Welding by Ultra-Short Laser Pulses", *International Journal of Extreme Manufacturing*, Vol. 1, No. 4, p. 042001, 2019.

109. Miyamoto, I., Y. Okamoto, R. Tanabe, Y. Ito, K. Cvecek and M. Schmidt, "Mechanism of Dynamic Plasma Motion in Internal Modification of Glass by fs-Laser Pulses at High Pulse Repetition Rate", *Optics Express*, Vol. 24, No. 22, pp. 25718–25731, 2016.